

Impact of grids and dynamical cores in CESM2.2 on the surface mass balance of the Greenland Ice Sheet

Adam R. Herrington¹, Peter H. Lauritzen¹, Marcus Lofverstrom², William H. Lipscomb¹, Andrew Gettelman¹ and Mark A. Taylor³

¹National Center for Atmospheric Research, 1850 Table Mesa Drive, Boulder, Colorado, USA

²Department of Geosciences, University of Arizona, 1040 E. 4th Street, Tucson, Arizona USA

³Sandia National Laboratories, Albuquerque, New Mexico, USA

Key Points:

- The CESM2.2 release includes several enhancements to the spectral-element dynamical core, including two Arctic refined mesh configurations.
- Quasi-uniform unstructured** grids degrade the Greenland Ice Sheet mass balance compared to latitude-longitude grids, **at the conventional 1° resolution**.
- The refined Arctic meshes substantially improve the surface mass balance over **conventional grid resolutions**.

15 **Abstract**

16 Six different configurations, a mixture of grids and atmospheric dynamical cores
 17 available in the Community Earth System Model, version 2.2 (CESM2.2), are evaluated
 18 for their skill in representing the climate of the Arctic and the surface mass balance of
 19 the Greenland Ice Sheet (GrIS). The finite-volume dynamical core uses structured, latitude-
 20 longitude grids, whereas the spectral-element dynamical core is built on unstructured
 21 meshes, permitting grid flexibility such as quasi-uniform grid spacing globally. The 1°–
 22 2° latitude-longitude and quasi-uniform unstructured grids systematically overestimate
 23 both accumulation and ablation over the GrIS. Of these 1°–2° grids, the latitude-longitude
 24 grids outperform the quasi-uniform unstructured grids because they have more degrees
 25 of freedom to represent the GrIS. Two Arctic-refined meshes, with 1/4° and 1/8° refine-
 26 ment over Greenland, were developed for the spectral-element dynamical core and are
 27 documented here as newly supported configurations in CESM2.2. The Arctic meshes sub-
 28 stantly improve the simulated clouds and precipitation rates in the Arctic. Over Green-
 29 land, these meshes skillfully represent accumulation and ablation processes, leading to
 30 a more realistic GrIS surface mass balance. As CESM is in the process of transitioning
 31 away from conventional latitude-longitude grids, these new Arctic-refined meshes improve
 32 the representation of polar processes in CESM by recovering resolution lost in the tran-
 33 sition to quasi-uniform grids, albeit at increased computational cost.

34 **Plain Language Summary**

35 The mass balance of Earth's big ice sheets is crucially important for understand-
 36 ing controls on global sea-level rise. However, the scale of the processes needed to rep-
 37 resent ice sheet mass balance is challenging to resolve in conventional Earth System Mod-
 38 els. This study evaluates the ability of different grids and atmospheric solvers (i.e., the
 39 dynamical core) in CESM2.2 to resolve the surface mass balance (SMB) of the Green-
 40 land Ice Sheet. We show that the ongoing transition away from latitude-longitude grids,
 41 towards quasi-uniform unstructured grids in CESM2.2 leads to a degradation of the sim-
 42 ultated SMB. Two variable-resolution grids with enhanced resolution over Greenland are
 43 developed and incorporated into the release of CESM2.2, which substantially improves
 44 the SMB over the latitude longitude grids.

45 **1 Introduction**

46 General Circulation Models (GCMs) are powerful tools for understanding the me-
 47 teorology and climate of the high latitudes, which are among the most sensitive regions
 48 on Earth to global and environmental change. GCMs differ vastly in their numerical treat-
 49 ment of polar regions because of the so-called *pole problem* (Williamson, 2007). The pole
 50 problem refers to numerical instability arising from the convergence of meridian lines into
 51 polar singularities on latitude-longitude grids (e.g., Figure 1a, hereafter referred to as
 52 *lat-lon* grids). Depending on the numerics, methods exist to suppress this instability, and
 53 lat-lon grids may be advantageous for polar processes by representing structures with
 54 finer resolution than elsewhere in the computational domain. With the recent trend to-
 55 wards quasi-uniform unstructured grids, any potential benefits of lat-lon grids in polar
 56 regions may be lost (hereafter, *quasi-uniform* refers to approximately isotropic grids, in
 57 contrast to lat-lon grids, which are highly anisotropic due to the polar singularity). In
 58 this study, we evaluate a number of grids and dynamical cores (hereafter referred to as
 59 *dycores*) available in the Community Earth System Model, version 2.2 (CESM2.2; Dan-
 60 abasoglu et al., 2020), including new variable-resolution grids (i.e., grids with enhanced
 61 resolution over a particular region), to understand their impacts on the simulated Arctic
 62 climate. We focus specifically on the climate and surface mass balance of the Green-
 63 land Ice Sheet.

In the 1970s, the pole problem was largely defeated through the adoption of efficient spectral transform methods in GCMs (see Williamson, 2007, and references therein). These methods transform grid point fields into a global, isotropic representation in wave space, where linear operators (e.g., horizontal derivatives) in the (truncated) equation set can be solved exactly. While spectral transform methods are still used today, local numerical methods have become desirable for their ability to run efficiently on massively parallel systems. The pole problem has thus re-emerged in contemporary climate models that use lat-lon grids, and some combination of reduced grids (modified lat-lon grids, with cells near the polar singularity elongated in the zonal direction) and polar filters are necessary to ameliorate this numerical instability (Jablonowski & Williamson, 2011). Polar filters subdue the growth of unstable computational modes by applying additional damping to the numerical solution over polar regions. This damping reduces the effective resolution in polar regions such that the resolved scales are *approximately* the same everywhere on the grid. We emphasize *approximately*, since it is conceivable that marginal increases in effective resolution occur over polar regions in lat-lon grids, despite polar filtering, since resolved waves can be represented with more grid points than at lower latitudes.

Dycores built on lat-lon grids have some advantages over [dycores built on](#) unstructured grids. Lat-lon coordinate lines are orthogonal, and aligned with zonally symmetric circulations that characterize many large-scale features of Earth's atmosphere. Lauritzen et al. (2010) has experimented with rotating lat-lon models such that their coordinate lines no longer align with an idealized, zonally balanced circulation. For the finite-volume lat-lon dycore considered in this paper (hereafter *FV*), numerical errors were shown to be largest when the polar singularity is rotated into the baroclinic zone (45°N latitude), generating spurious wave growth much earlier in the simulation than for other rotation angles. This illustrates the advantages of coordinate surfaces aligned with latitude bands, albeit an extreme example where the polar singularity and the polar filter are also contributing to the spurious wave growth. The unstructured grids all generate spurious baroclinic waves earlier in the simulations than the (unrotated) lat-lon models, although the unstructured model considered in this paper, the spectral-element dycore (hereafter *SE*), holds a balanced zonal flow without spurious wave growth appreciably longer than the rotated FV experiments (Lauritzen et al., 2010). And unlike FV, the SE dycore has the same error characteristics regardless of how the grid is rotated.

The polar filter in the FV model impedes efficiency at large processor (CPU) counts because it requires a spectral transform, which [has a](#) large communication overhead (Suarez & Takacs, 1995; Dennis et al., 2012). Unstructured grids support quasi-uniform grid spacing globally, and there is no pole problem (e.g., Figure 1c). [This is in part why](#) unstructured grids are becoming more common; their improved performance on massively parallel systems and lack of constraints on grid structure (Taylor et al., 1997; Putman & Lin, 2007; Wan et al., 2013). This increased grid flexibility allows for the adoption of variable-resolution grids (e.g., Figure 2; hereafter abbreviated as *VR*), sometimes referred to as regional grid refinement. In principle, grid refinement over polar regions can make up for any loss of resolution in transitioning away from lat-lon grids (e.g., Figure 2). However, local grid refinement comes at the cost of a smaller CFL-limited time step in the refined region; the CFL-condition — short for Courant–Friedrichs–Lowy condition — is a necessary condition for numerical stability when using discrete data in time and space.

We emphasize that the pole problem is a distinctive feature of the dycore in atmospheric models. Polar filters do not directly interfere with the physical parameterizations, nor do they have any bearing on the surface models; e.g., the land model can take full advantage of the greater number of grid cells in polar regions on lat-lon grids. This is particularly relevant for the surface mass balance ([SMB; the integrated sum of precipitation and runoff](#)) of the Greenland Ice Sheet, which relies on hydrological processes represented in the land model.

The SMB of the Greenland Ice Sheet (hereafter *GrIS*) is determined by processes occurring over a range of scales that are difficult to represent in GCMs (Pollard, 2010). GrIS precipitation is concentrated at the ice-sheet margins, where steep topographic slopes drive orographic precipitation. The truncated topography used by low resolution GCMs enables moisture to penetrate well into the GrIS interior, manifesting as a positive precipitation bias [in the interior](#) (Pollard & Groups, 2000; Van Kampenhout et al., 2019). GrIS ablation areas ([marginal regions where the annual SMB is negative](#)) are typically less than 100 km wide and are confined to low-lying areas or regions with low precipitation. These narrow ablation zones are not fully resolved in low-resolution GCMs, and may further degrade the simulated SMB. [More recently, GCMs such as CESM and the NASA Goddard Institute for Space Studies GCM \(Alexander et al., 2019\), have implemented an elevation class downscaling scheme for computing the SMB. The downscaling helps to resolve to these narrow ablation zones in GCMs \(Sellevold et al., 2019\), but large SMB biases remain.](#) For example, CESM, version 2.0 (CESM2) underestimates ablation in the northern GrIS, leading to unrealistic ice advance when run with an interactive ice sheet component (Lofverstrom et al., 2020).

Regional climate models (RCMs) are commonly relied upon to provide more accurate SMB estimates. The limited area domain used by RCMs permits the use of high-resolution grids capable of resolving SMB processes, and can skillfully simulate the GrIS SMB (Box et al., 2004; Rae et al., 2012; Van Angelen et al., 2012; Fettweis et al., 2013; Mottram et al., 2017; Noël et al., 2018). However, unlike GCMs, RCMs are not a freely evolving system, and the atmospheric state must be prescribed at the lateral boundaries of the model domain. The inability of the RCM solution to influence larger-scale dynamics outside the RCM domain (due to the prescribed boundary conditions) severely limits this approach from properly representing the role of the GrIS in the climate system. In addition, the boundary conditions are derived from a separate host model, which introduces inconsistencies due to differences in model design between the host model and the RCM.

In order to retain the benefits of RCMs in a GCM, Van Kampenhout et al. (2019) used the VR capabilities of the SE dycore in CESM, generating [grids](#) where Greenland is represented with [up to](#) $1/4^\circ$ resolution, and elsewhere with the more conventional 1° resolution. The simulated SMB compared favorably to the SMB from RCMs and observations. The VR approach is therefore emerging as a powerful tool for simulating and understanding the GrIS and its response to different forcing scenarios.

The SE dycore has been included in the model since CESM version 1, but has been under active development ever since. This includes the switch to a dry-mass vertical coordinate (Lauritzen et al., 2018) and incorporation of an accelerated multi-tracer transport scheme (Lauritzen et al., 2017), made available in CESM2. This paper documents several additional enhancements to the SE dycore as part of the release of CESM2.2. These include three new VR configurations (Figure 2), two Arctic meshes and a Contiguous United-States mesh (**CONUS**; featured in Pfister et al. (2020)). While there are dozens of published studies using VR in CESM (e.g., Zarzycki et al., 2014; Rhoades et al., 2016; Gettelman et al., 2017; Burakowski et al., 2019; Bambach et al., 2021), these studies either used development code or collaborated closely with model developers. CESM2.2 is the first code release that contains out-of-the-box VR functionality.

This study compares the representation of Arctic regions using the SE and FV dycores in CESM2.2 (see description below), as these two dycores treat high latitudes (i.e., the pole problem) in different ways. Section 2 documents the grids, dycores, and physical parameterizations used in this study, and also describes the experiments, datasets, and evaluation methods. Section 3 analyzes the results of the experiments, and Section 4 provides a general discussion and conclusions.

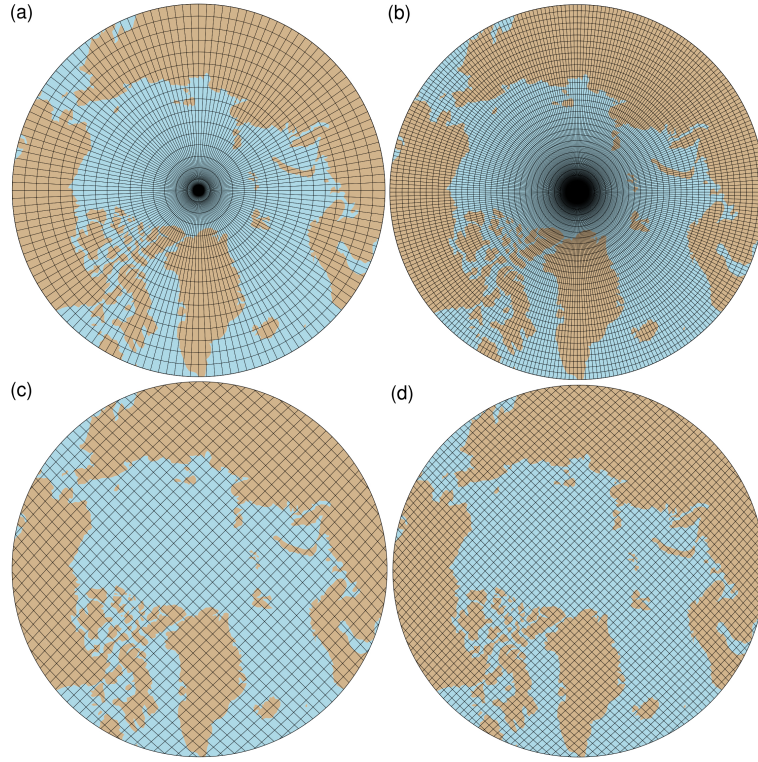


Figure 1. Computational grids for the 1° – 2° lat-lon and quasi-uniform unstructured grids in this study. Grids names after Table 1, (a) 2° lat-lon grid (f19), (b) 1° lat-lon grid (f09), (c) 1° quasi-uniform unstructured grid with reduced physics resolution (ne30pg2) and (d) 1° quasi-uniform unstructured grid (ne30pg3).

168 2 Methods

169 CESM2.2 is a CMIP6-class (Coupled Model Intercomparison Project Phase 6; Eyring
 170 et al., 2016) Earth System Model maintained by the National Center for Atmosphere Re-
 171 search. CESM2.2 contains sub-component models for the atmosphere, land, ocean, sea-
 172 ice, and land-ice, and can be configured to run with varying degrees of complexity. All
 173 simulations described in this study use an identical transient 1979-1998 Atmospheric Model
 174 Inter-comparison Project (AMIP) configuration, with prescribed monthly sea-surface tem-
 175 perature and sea ice following Hurrell et al. (2008). In CESM terminology, AMIP sim-
 176 ulations use the FHIST computational set and run out of the box in CESM2.2. The land-
 177 ice component is not dynamically active in FHIST. However, the surface mass balance
 178 is computed by the land model before being passed to the land-ice component; FHIST
 179 includes the functionality to simulate the surface mass balance of the Greenland Ice Sheet.

180 2.1 Dynamical cores

181 The atmospheric component of CESM2.2 (Danabasoglu et al., 2020), the Commu-
 182 nity Atmosphere Model, version 6.3 (CAM6; Gettelman et al., 2019; Craig et al., 2021),
 183 supports several different atmospheric dynamical cores. These include dycores on lat-
 184 lon grids, such as finite-volume (FV; Lin, 2004) and Eulerian spectral transform (EUL;
 185 Collins et al., 2006) models, and dycores built on unstructured grids, including spectral-
 186 element (SE; Lauritzen et al., 2018) and finite-volume 3 (FV3; Putman & Lin, 2007) mod-
 187 els. This study compares the performance of the SE and FV dycores, omitting the EUL

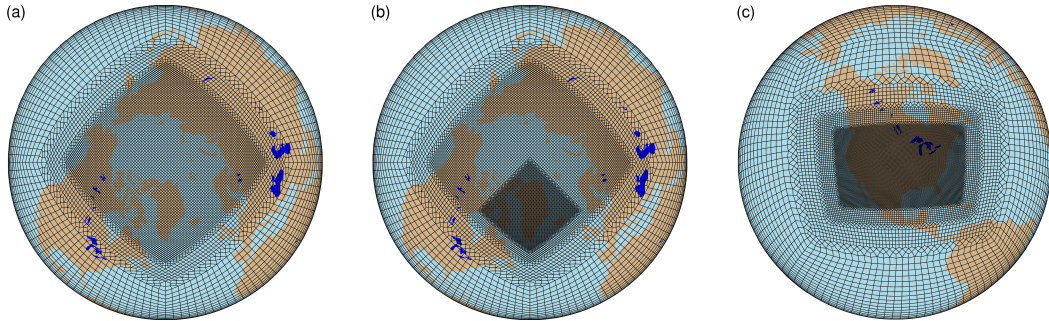


Figure 2. Variable-resolution grids available in CESM2.2, (a) **Arctic**, (b) **Arctic - GrIS** and (c) **CONUS**. Note what is shown is the element grid; the computational grid has 3×3 independent grid points per element.

and FV3 dycores. CESM2 runs submitted to CMIP6 used the FV dycore, whereas the SE dycore is often used for global high-resolution simulations (e.g., Small et al., 2014; Bacmeister et al., 2016; Chang et al., 2020) due to its higher throughput on massively parallel systems (Dennis et al., 2012).

2.1.1 Finite-volume (FV) dynamical core

The FV dycore integrates the [hydrostatic](#) equations of motion using a finite-volume discretization on a spherical lat-lon grid (Lin & Rood, 1997). The 2D dynamics evolve in floating Lagrangian layers that are periodically mapped to an Eulerian reference grid in the vertical (Lin, 2004). Hyperviscous damping is applied to the divergent modes, and is increased in the top few layers (referred to as a *sponge layer*) to prevent undesirable interactions with the model top, such as wave reflection (Lauritzen et al., 2011). A polar filter damps computational instability due to the convergence of meridians, permitting a longer time step. It takes the form of a Fourier filter in the zonal direction, with the damping coefficients increasing monotonically in the meridional direction (Suarez & Takacs, 1995). The form of the filter is designed to slow down the propagation of large zonal wave-numbers to satisfy the CFL condition of the shortest resolved wave at some reference latitude.

2.1.2 Spectral-element (SE) dynamical core

The SE dycore integrates the [hydrostatic](#) equations of motion using a high-order continuous Galerkin method (Taylor et al., 1997; Taylor & Fournier, 2010). The computational domain is a cubed-sphere grid ([A cubed-sphere grid is obtained by projecting each face of a cube onto a sphere](#)) tiled with quadrilateral elements (see Figure 2). Each element contains a fourth-order basis set in each horizontal direction, with the solution defined at the roots of the basis functions, the Gauss-Lobatto-Legendre quadrature points. This results in 16 nodal points per element, with 12 of the points lying on the (shared) element boundary. Communication between elements uses the direct stiffness summation (Canuto et al., 2007), which applies a numerical flux to the element boundaries to reconcile overlapping nodal values and produce a continuous global basis set.

As with the FV dycore, the dynamics evolve in floating Lagrangian layers that are subsequently mapped to an Eulerian reference grid. A dry mass vertical coordinate was recently implemented for thermodynamic consistency with condensates (Lauritzen et al., 2018). The 2D dynamics have no implicit dissipation, and so hyperviscosity operators

220 are applied to all prognostic variables to remove spurious numerical errors (Dennis et
221 al., 2012). Laplacian damping is applied in the sponge layer.

222 SE is a next generation of dycore, and is less mature than the FV dycore due to
223 its shorter history. In CESM2.2, the SE numerics have been enhanced relative to CESM2.0
224 to mitigate spurious noise over topography. These algorithmic changes are described in
225 Appendix A. Future versions of CESM will likely continue to include further optimiza-
226 tions and enhancements to the (nascent) SE dycore.

227 The SE dycore supports regional grid refinement via its VR configuration, requir-
228 ing two enhancements over quasi-uniform resolution grids. First, as the numerical vis-
229 cosity increases with resolution, explicit hyperviscosity relaxes according to the local el-
230 ement size, reducing in strength by an order of magnitude per halving of the grid spac-
231 ing. A tensor-hyperviscosity formulation is used (Guba et al., 2014), which adjusts the
232 coefficients in two orthogonal directions to more accurately target highly distorted quadri-
233 lateral elements. Second, the topography boundary conditions are smoothed in a way
234 that does not excite grid scale modes, and so the NCAR topography software (Lauritzen
235 et al., 2015) has been modified to scale the smoothing radius by the local element size,
236 resulting in rougher topography in the refinement zone.

237 When using the SE dycore with quasi-uniform grid spacing, the SE tracer trans-
238 port scheme is replaced with the Conservative Semi-Lagrangian Multi-tracer transport
239 scheme (CSLAM) (Lauritzen et al., 2017). Atmospheric tracers have large, nearly dis-
240 continuous horizontal gradients that are difficult to represent with spectral methods, which
241 are prone to oscillatory “Gibbs-ringing” errors (Rasch & Williamson, 1990). CSLAM has
242 improved tracer property preservation and accelerated multi-tracer transport. It uses a
243 separate grid from the spectral-element dynamics, dividing each element into 3×3 con-
244 trol volumes with quasi-equal area. The physical parameterizations are computed from
245 the state on the CSLAM grid, which has clear advantages over the original SE dycore
246 in which the physics are evaluated at Gauss-Lobatto-Legendre points (Herrington et al.,
247 2018). CSLAM advection is not an available option in the VR configuration, which in-
248 stead uses the standard SE tracer transport scheme with the physics evaluated at Gauss-
249 Lobatto-Legendre points.

250 2.2 Physical parameterizations

251 All simulations in this study use the CAM6 physical parameterization package (hereafter
252 referred to as the *physics*; Gettelman et al., 2019). The physics in CAM6 differs from
253 its predecessors through the incorporation of high-order turbulence closure, Cloud Lay-
254 ers Unified by Binormals (CLUBB; Golaz et al., 2002; Bogenschutz et al., 2013), which
255 jointly acts as a planetary boundary layer, shallow convection, and cloud macrophysics
256 scheme. CLUBB is coupled with the MG2 microphysics scheme (Gettelman & Morri-
257 son, 2015; Gettelman et al., 2015), which computes prognostic precipitation and uses clas-
258 sical nucleation theory to represent cloud ice for improved cloud-aerosol interactions. Deep
259 convection is parameterized using a convective quasi-equilibrium mass flux scheme (Zhang
260 & McFarlane, 1995; Neale et al., 2008) and includes convective momentum transport (Richter
261 et al., 2010). Boundary layer form drag is modeled after Beljaars et al. (2004), and orog-
262 graphic gravity wave drag is represented with an anisotropic method informed by the
263 orientation of topographic ridges at the sub-grid scale (the ridge orientation is derived
264 from a high-resolution, global topography dataset (J. J. Danielson & Gesch, 2011)).

265 Initial simulations with the SE dycore produced weaker shortwave cloud forcing
266 relative to the tuned finite-volume dycore in the standard CESM2 configuration. The
267 SE dycore in CESM2.2 therefore has two CLUBB parameter changes to provide more
268 realistic cloud forcing and top-of-atmosphere radiation balance. We reduced the width
269 of the sub-grid distribution of vertical velocity (`clubb_gamma` = 0.308 → 0.270) and
270 also reduced the strength of the damping for horizontal component of turbulent energy

grid name	dycore	Δx_{eq} (km)	Δx_{fine} (km)	Δt_{phys} (s)	cost(25 nodes)	cost(50 nodes)
f19	FV	278	-	1800	436.66	-
f09	FV	139	-	1800	1534.57	2024.24
ne30pg2	SE-CSLAM	167	-	1800	1497.26	1683.97
ne30pg3	SE-CSLAM	111	-	1800	1890.48	2090.43
ne30pg3*	SE-CSLAM	111	-	450	-	-
Arctic	SE	111	28	450	15947.41	16675.45
Arctic – GrIS	SE	111	14	225	40305.03	41036.67

Table 1. Grids and dycores used in this study. Δx_{eq} is the average equatorial grid spacing, Δx_{fine} is the grid spacing in the refined region (if applicable), and Δt_{phys} is the physics time step. FV refers to the finite-volume dycore, SE the spectral-element dycore, and SE-CSLAM the spectral-element dycore with CSLAM tracer advection. The FV dycore uses lat-lon grids, whereas the SE and SE-CSLAM dycores run on unstructured grids. We use the ne30pg3 grid for two runs with different values of Δt_{phys} . The last columns provide the computational costs in core hours per simulated year (CHPSY). The costs are from single month runs using 25 nodes and 50 nodes on the Cheyenne supercomputer (Computational and Information Systems Laboratory, 2017).

(`clubb_c14` = 2.2 → 1.6) to increase cloudiness. For a description of how CLUBB parameters impact the simulated climate, see Guo et al. (2015).

2.3 Grids

We evaluate model simulations on six different grids in this study (Table 1). The FV dycore is run with nominal 1° and 2° grid spacing, referred to as f09 and f19, respectively (Figure 1a,b). We also run the 1° equivalent of the SE-CSLAM grid, referred to as ne30pg3 (Figure 1d), where *ne* refers to a grid with *ne* × *ne* quadrilateral elements per cubed-sphere face, and *pg* denotes that there are *pg* × *pg* control volumes per element for computing the physics. We run an additional 1° SE-CSLAM simulation with the physical parameterizations computed on a grid with 2 × 2 control volumes per element, ne30pg2 (Figure 1c; Herrington et al., 2019, note CSLAM is still run on the 3 × 3 control volume grid).

Three VR meshes were developed for the CESM2.2 release to support grid refinement over the Arctic and the United States (Figure 2). This paper serves as the official documentation of these grids. The VR meshes were developed using the software package SQuadgen (<https://github.com/ClimateGlobalChange/squadgen>). The Arctic grid is a 1° grid with 1/4° regional refinement over the broader Arctic region (when using degrees to describe the resolution of unstructured grids, degrees refers to degrees at the equator). The Arctic–GrIS grid is identical to the Arctic grid, but with an additional patch covering the island of Greenland with 1/8° resolution. The CONUS grid contains 1/8° refinement over the United States, and 1° everywhere else. The CONUS grid is not discussed any further in this paper; see Pfister et al. (2020) for simulations with the CONUS grid.

The accuracy of the simulated surface mass balance is expected to be sensitive to grid resolution. Figure 3a shows the average grid spacing over the Greenland Ice Sheet (*GrIS* hereafter), in all six grids, as well as two grids pertaining to the Regional Atmospheric Climate Model (RACMO; Noël et al., 2018, 2019), which are used for validation purposes in this study (Table 2). The ne30pg2 grid has the coarsest representation with an average grid spacing (Δx) of $\Delta x = 160$ km, and the Arctic – GrIS grid has the highest resolution with an average grid spacing of $\Delta x = 14.6$ km, similar to the 11 km grid spacing of the RACMO2.3 grid. The ne30pg3 grid has an average $\Delta x = 111.2$ km,

302 substantially coarser than the **f09** grid, with an average $\Delta x = 60$ km. Although **ne30pg3**
 303 and **f09** have similar average grid spacing over the entire globe, and comparable com-
 304 putational costs, the convergence of meridians on the FV grid enhances the resolution
 305 over the GrIS. The **Arctic** grid has an average grid spacing of $\Delta x = 27.8$ km.

306 The physics time step depends on the grid resolution. Increased horizontal reso-
 307 lution permits faster vertical velocities that reduce characteristic time scales, so the physics
 308 time step is reduced to avoid large time truncation errors (Herrington & Reed, 2018).
 309 The **Arctic** and **Arctic – GrIS** grids are run with a $4\times$ and $8\times$ reduction in physics
 310 time step relative to the default 1800 s time step used in the 1° and 2° grids (Table 1).

311 All grids and dycores in this study use 32 hybrid pressure-sigma levels in the ver-
 312 tical, with a model top of 2 hPa or about 40 km. However, any grid or dycore can in prin-
 313 ciple be run with a higher model top or finer vertical resolution.

314 2.4 Computational costs

315 The last columns of Table 1 provides cost estimates for the different grids and dy-
 316 cores. The costs, expressed as core hours per simulated year (CHPSY), are taken from
 317 single month runs of FHIST, with no i/o, and using 25 nodes (900 tasks) and 50 nodes
 318 (1800 tasks) on the Cheyenne supercomputer (Computational and Information Systems
 319 Laboratory, 2017). 25 nodes is on the low side for a typical multi-decadal climate sim-
 320 ulation at 1° resolution, but it's the largest number of tasks that can be supported by
 321 the **f19** grid, and we chose to fix the number of tasks across all grids for the purposes
 322 of comparing their costs. We also provide costs using 50 nodes, excluding **f19**, to pro-
 323 vide a more practical cost estimate for longer climate integrations. There are probably
 324 better approaches for comparing costs across different grids and dycores, e.g., holding
 325 fixed the number of grid columns per task, but it is beyond the scope of this study.

326 The cheapest grid is the **f19** grid at 436.66 CHPSY, as this is the only grid run-
 327 ning with 2° dynamics. The **f09** grid costs 1534.57 CHPSY using 25 nodes, which is no-
 328 ticeably cheaper than **ne30pg3** at 1890.48 CHPSY. The **ne30pg2** grid is 20% cheaper than
 329 the **ne30pg3** grid, in both the 25 node and 50 node runs, consistent with previous es-
 330 timates (Herrington & Reed, 2018). The FV model is known to be cheaper than SE at
 331 small core counts, whereas SE is more efficient than FV at large core counts due to its
 332 improved scalability (Dennis et al., 2005, 2012). In the more conventional 50 node runs,
 333 **f09** costs are much more similar to **ne30pg3**, due to a 30% cost increase in **f09** relative
 334 to the 25 node run (Table 1). The **Arctic** grid is an order of magnitude more expen-
 335 sive than the lat-lon and quasi-uniform grids, at about 16k CHPSY, whereas the **Arctic–**
 336 **GrIS** grid is a more than twice that (40k CHPSY). Note that all timing numbers are from
 337 runs without threading. The **f09** grid is the only grid that runs out-of-the-box with thread-
 338 ing; holding the number of tasks fixed leads to a 4%–6.5% reduction in CHPSY com-
 339 pared to runs without threading.

340 2.5 Simulated surface mass balance (SMB)

341 CESM simulates the GrIS SMB as the sum of ice accumulation and ice ablation.
 342 The latter contains contributions from sublimation and liquid runoff from ice melt. Liq-
 343 uid precipitation and liquid runoff may also contribute to ice accumulation by penetrat-
 344 ing pore spaces in the snowpack/firn layer and freeze, forming ice lenses. These relevant
 345 SMB processes are represented by different CESM components, but it is the Commu-
 346 nity Land Model, version 5 (CLM; Lawrence et al., 2019), that aggregates these processes
 347 and computes the SMB.

348 CLM runs on the same grid as the atmosphere, and uses a downscaling technique
 349 to account for sub-grid variability in SMB. In short, the ice sheet patch in a CLM grid
 350 cell is subdivided into 10 elevation classes (ECs), each with a distinct surface energy bal-

351 ance and SMB. The area fraction of each EC is computed from the CISM initial con-
 352 ditions, which are based on a high-resolution dataset of the observed, modern extent and
 353 thickness of the GrIS (Morlighem et al., 2014). Note that for configurations with a dy-
 354 namically active ice sheet, the area fractions are continuously updated throughout the
 355 run to reflect the evolving ice sheet geometry in CISM. The near-surface air tempera-
 356 ture, humidity, and air density are calculated for each EC using an assumed lapse rate
 357 and the elevation difference from the grid-cell mean. Precipitation from CAM is repar-
 358 titioned into solid or liquid based on the surface temperature of the EC; precipitation
 359 falls as snow for temperatures between $T < -2^{\circ}$ C, as rain for $T > 0^{\circ}$ C, and as a lin-
 360 ear combination of rain and snow for temperatures between -2° C and 0° C.

361 Changes in ice depth, not snow depth, count toward the SMB. Snow accumulation
 362 in each EC is limited to a depth of 10 m liquid water equivalent. Any snow above the
 363 10 m cap contributes towards ice accumulation, and refreezing of liquid water within the
 364 snowpack is an additional source of ice. Surface ice melting (after melting of the over-
 365 lying snow) yields a negative SMB. Integrating over all ECs, weighting by the area frac-
 366 tions, provides a more accurate SMB than would be found using the grid-cell mean el-
 367 evation. For a more detailed description of how the SMB is computed in CESM, we re-
 368 fer the reader to Lipscomb et al. (2013); Sellevold et al. (2019); van Kampenhout et al.
 369 (2020); Muntjewerf et al. (2021).

370 Since snow in the accumulation zone must reach the cap to simulate a positive SMB,
 371 the snow depths on the VR grids were spun up by forcing CLM in standalone mode, cy-
 372 cling over data from a 20-year Arctic FHIST simulation ([with perpetual 1979 bound-](#)
 373 [ary conditions](#)) for about 500 years. The 1° – 2° lat-lon and quasi-uniform unstructured
 374 grids are initialized with the SMB from an existing f09 spun-up initial condition.

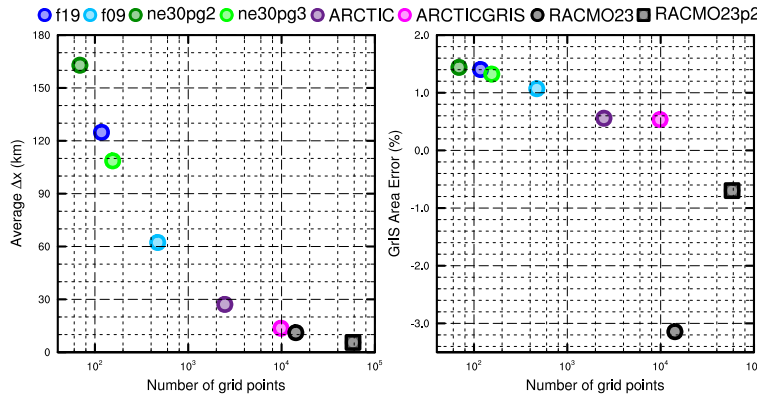
375 2.6 Validation Datasets

376 We use several [validation](#) datasets (Table 2) to assess the performance of the sim-
 377 ulations. The ERA5 reanalysis product (Copernicus, 2019) is used for validating the large-
 378 scale circulation and extreme precipitation events. Clouds and radiation fields are val-
 379 idated using remote sensing products, the CERES-EBAF ED4.1 (Loeb et al., 2018) and
 380 the CALIPSO-GOCCP (Chepfer et al., 2010) datasets, respectively. We also utilize a
 381 MODIS GrIS surface albedo product, mapped to a 25 km regional climate model grid
 382 (Tedesco & Alexander, 2013).

383 SMB datasets are gathered from multiple sources. RACMO, version 2.3 11km (RACMO23;
 384 Noël et al., 2015) and version 2.3p2 5.5km (RACMO2.3p2; Noël et al., 2018, 2019) are
 385 RCM simulations targeting Greenland, forced by ERA renalyses products at the domain's
 386 lateral boundaries. The RACMO simulations have been shown to perform skillfully against
 387 observations and are often used as modeling targets (e.g., Evans et al., 2019; van Kam-
 388 penhout et al., 2020). The RACMO datasets are used along with the CERES-EBAF prod-
 389 uct to validate the radiative fluxes around Greenland.

390 In-situ SMB (snow pit and ice cores) and [remote sensing datasets](#) (e.g., IceBridge
 391 radar accumulation dataset) are maintained in The Land Ice Verification and Validation
 392 toolkit (LIVVkit), version 2.1 (Evans et al., 2019). However, these point-wise measure-
 393 ments are difficult to compare to model output spanning several different grids, especially
 394 since the SMB from each elevation class is not available from the model output. We used
 395 a nearest-neighbor technique for an initial analysis, which showed that the model biases
 396 are similar to those computed using the RACMO datasets. Because of the uncertainty
 397 of comparing gridded fields to point-wise measurements, and the lack of information added
 398 with regard to model biases, we omitted these datasets from our analysis.

data product	years used in this study	resolution	citation
ERA5	1979-1998	1/4°	Copernicus (2019)
CERES-EBAF ED4.1	2003-2020	1°	Loeb et al. (2018)
CALIPSO-GOCCP	2006-2017	2°	Chepfer et al. (2010)
MODIS-MAR	2000-2013	25 km	Tedesco and Alexander (2013)
RACMO2.3	1979-1998	11 km	Noël et al. (2015)
RACMO2.3p2	1979-1998	5.5 km	Noël et al. (2019)

Table 2. Description of validation datasets used in this study.**Figure 3.** The spatial properties of the GrIS as represented by different grids in this study. (Left) approximate average grid spacing over GrIS, (right) GrIS area error, computed as the relative differences from the reference dataset described in the text. Also included are the two RACMO grids used for validation (see Table 2).

399

2.7 SMB Analysis

We seek to integrate SMB components over a GrIS ice mask and to diagnose their contributions to the GrIS mass budget. However, the ice masks vary across the grids, especially in comparison to the RACMO3.2 ice mask, whose total area is about 3% less than that of the reference dataset (i.e., the GrIS initial conditions in CISM; Figure 3b). CLM's dataset creation tool generates the model ice mask by mapping the reference dataset to the target grid using the Earth System Modeling Framework (ESMF) first-order conservative remapping algorithm (Team et al., 2021). The figure suggests that the mapping errors are less than 1.5% across the CESM2.2 grids. The area errors in Figure 3b may seem small, but even 1–2% area differences can lead to large differences in integrated SMB (Hansen et al., 2022).

We have taken a common-ice-mask approach by mapping all model fields to the lowest-resolution grids, i.e., the **f19** and **ne30pg2** grids, and integrating over these low-resolution ice masks. The use of low-resolution common ice masks is a conservative decision, and is justified because we seek to use first-order remapping algorithms to map fields to the common ice mask, which is not generally reliable when mapping to a higher-resolution grid than the source grid. We use two remapping algorithms: ESMF first-order conservative and the TempestRemap (Ullrich & Taylor, 2015) high-order monotone algorithm. Since mapping errors are sensitive to grid type, we evaluate all quantities on both common ice masks, the **f19** and **ne30pg2** masks. Thus, we evaluate an integrated quantity on a given grid up to four times to estimate the uncertainty due to differences in grid type and remapping algorithms.

421 The SMB is expressed in a form that is agnostic of water phase, a total water mass
 422 balance, to facilitate comparisons across different grids with different ice masks and to
 423 increase consistency with the variables available in the RACMO datasets. The SMB for
 424 total water can be expressed as:

$$\text{SMB} = \text{accumulation} + \text{runoff} + \text{evaporation} + \text{sublimation}, \quad (1)$$

425 where all terms have consistent sign conventions (positive values contribute mass, and
 426 negative values reduce mass). The accumulation source term refers to the combined solid
 427 and liquid precipitation, runoff refers to the liquid water sink, and evaporation/sublimation
 428 is the vapor sink. Since the runoff term aggregates many processes, we isolate the melt-
 429 ing contribution by also tracking the combined melt of snow and ice.

430 The total water SMB (equation 1) is different from the SMB internally computed
 431 by CLM and described in section 2.5, which only tracks ice mass. We do not use CLM's
 432 internally computed SMB in this study. Rather, we utilize the components of the inter-
 433 nally computed SMB to construct the total water SMB.

434 We consider two approaches for mapping and integrating the SMB components over
 435 the common ice masks:

- 436 1. Map the grid-cell mean quantities to the common grid, and integrate the mapped
 437 fields over the common ice masks.
- 438 2. Map the patch-level quantities (i.e., the state over the ice fractional component
 439 of the grid cell) to the common grid, and integrate the mapped fields over the com-
 440 mon ice masks.

441 Note that we are mapping to low-resolution grids that have larger GrIS areas than
 442 the source grids (Figure 3b). Since the components of equation 1 are not confined to the
 443 ice mask, method 1 reconstructs the SMB over the portion of the common ice mask that
 444 is outside the ice mask on the source grid. While this may be a an acceptable way to re-
 445 construct the mass source terms over different ice masks, ice melt is zero outside the source
 446 ice mask, and so method 1 will underestimate the mass sink term. This underestima-
 447 tion is systematic in method 2, where all variables are exclusive to the ice mask; map-
 448 ping to a lower-resolution grid will dilute a field of non-zero values over the ice mask with
 449 a field of zeros outside the ice mask. However, patch-level values for processes exclusive
 450 to the ice mask (e.g., ice melt) will on average have larger magnitudes than the grid-mean
 451 quantities used in method 1.

452 The different error characteristics of the two methods are used to further diversify
 453 the ensemble. Each of the four regridding combinations (with conservative and high-order
 454 remapping to the f09 and ne30pg2 grids) are repeated with each method, resulting in
 455 (up to) eight values for each integrated quantity. Unfortunately, the patch-level values
 456 of evaporation/sublimation are not available from the model output, and we estimate
 457 their contribution by zeroing out the field for grid cells that have no ice, prior to map-
 458 ping to the common ice mask. This will degrade the SMB estimates using method 2, but
 459 we are more interested in characterizing the behavior of individual processes across grids
 460 and dycores, expressed as the components of the SMB, rather than the SMB itself.

461 3 Results

462 3.1 Tropospheric temperatures

463 Before delving into the simulated Arctic climate conditions, we assess the global
 464 mean differences between the various grids and dycores. Figure 4 shows 1979-1998 an-
 465 nual mean, zonal mean height plots of temperature, expressed as differences between 1°–
 466 2° lat-lon and quasi-uniform unstructured grids and dycores. The f09 grid is warmer

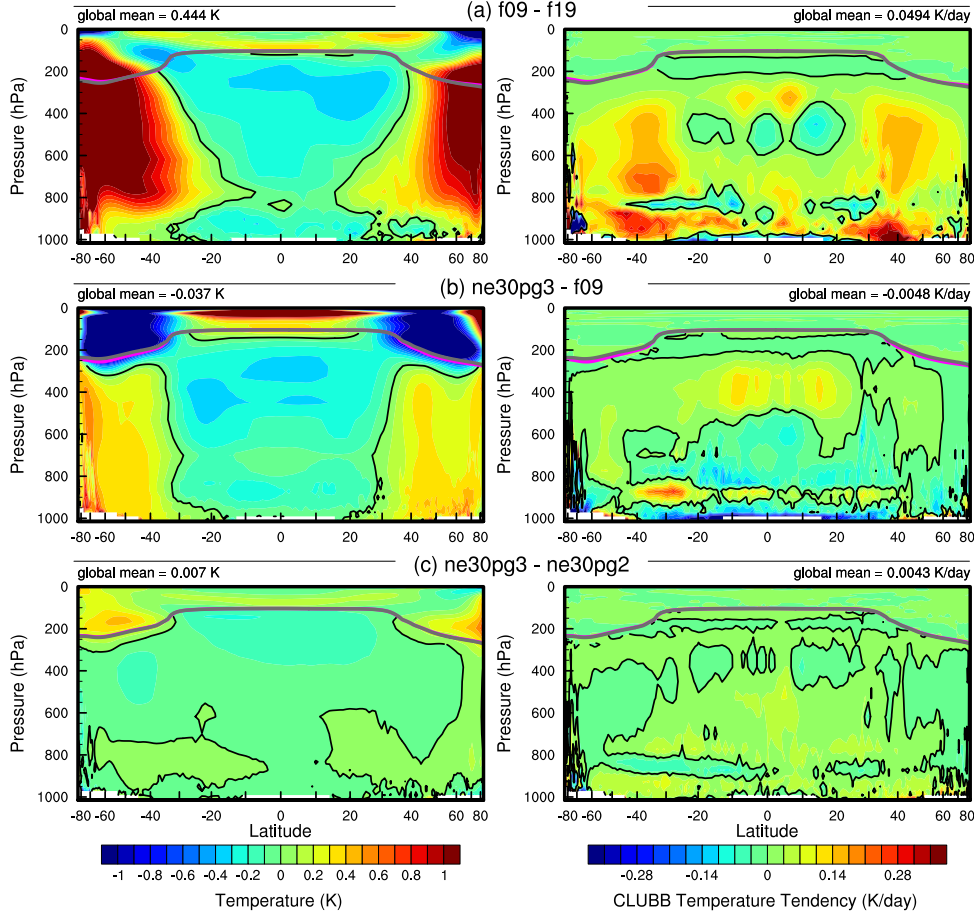


Figure 4. 1979–1998 annual mean temperature (left column) and CLUBB temperature tendencies (right column) in zonal mean height space, expressed as differences between the various $1^{\circ} - 2^{\circ}$ grids. The thick grey and magenta lines are the tropopause for the control run and the test run, respectively.

than the f19 grid, primarily in the mid-to-high latitudes throughout the depth of the troposphere. This is a common response to increasing horizontal resolution in GCMs (Pope & Stratton, 2002; Roeckner et al., 2006). Herrington and Reed (2020) have shown that this occurs in CAM due to higher resolved vertical velocities which, in turn, generate more condensational heating in the CLUBB macrophysics. The right panel in Figure 4a supports this interpretation, showing an increase in the climatological CLUBB heating at all latitudes in the f09 grid, but with the largest increase in the mid-latitudes.

As the SE dycore is less diffusive than the FV dycore, the resolved vertical velocities are larger in the SE dycore, and so the ne30pg3 troposphere is modestly warmer than f09 (Figure 4b). The stratosphere responds differently, with ne30pg3 much cooler than f09 in the mid-to-high latitudes. Figure 4c also shows small temperature differences between ne30pg3 and ne30pg2, with ne30pg3 slightly warmer near the tropopause at high latitudes. This is consistent with the similar climates found for these two grids by Herrington et al. (2019).

Comparing the VR grids to the [lat-lon](#) and [quasi-uniform](#) grids is complicated because we simultaneously increase the resolution and reduce the physics time-step, both

of which influence the solution (Williamson, 2008). We therefore run an additional `ne30pg3` simulation with the shorter physics time step used in the `Arctic` grid (450 s), referred to as `ne30pg3*` (Table 1). Figure 5a shows the difference between `ne30pg3*` and `ne30pg3` for climatological summer temperatures in zonal-mean height space. The troposphere is warmer with the reduced time step, and the mechanism is similar in that the shorter time step increases resolved vertical velocities (not shown) and CLUBB heating (right panel in Figure 5a). Figure 5b shows the difference in climatological summer temperature between the `Arctic` grid and the `ne30pg3*` grid. With the same physics time step, the greater condensational heating and warmer temperatures are confined to the refined Arctic region.

We note that there is not perfect alignment of the CLUBB heating anomalies and the temperature anomalies in Figures 4 & 5. This leaves some uncertainty as to whether CLUBB is solely responsible for the temperature anomalies caused by changing grid resolution or dycore, as asserted above. In the deep Tropics, gravity waves are expected to propagate temperature anomalies far from their heating source, and so the misalignment is less troublesome for this region. In the mid-latitudes, we speculate that this misalignment is due to averaging the CLUBB heating over all time. Herrington and Reed (2020) have shown that only the CLUBB heating coinciding with upward resolved vertical velocities tends to align spatially with the temperature response, whereas heating anomalies associated with descending grid columns had no alignment with the temperature response. Therefore the average over all time will dilute the heating signal, and potentially lead to misalignments between the heating rates and temperature anomalies.

Figure 5c shows that the `Arctic-GrIS` grid is much warmer than the `Arctic` grid in the Arctic summer. This may be due, in part, to the shorter physics time step, but the temperature response is too large to be explained by enhanced condensational heating from CLUBB alone. This summer warming appears to be a result of variations in the stationary wave pattern, with a swath of anomalous southerly winds to the west of Greenland (not shown). This dynamic response is interesting, because other than the physics time step, the only difference between the `Arctic - GrIS` and `Arctic` runs is the doubling of resolution over Greenland. This behavior will be explored further in a future study.

Keeping our focus on the Arctic region, and in particular Greenland, it is useful to understand summer temperature biases due to their control on ice and snow melt over the GrIS (Ohmura, 2001). Figure 6 shows the 1979–1998 lower troposphere summer temperature bias relative to ERA5, computed by equating a layer mean virtual temperature with the 500–1000 hPa geopotential thickness. The results are consistent with the zonal mean height plots; increasing resolution from `f19` to `f09` warms the climate, and the 1° SE grids are warmer than the FV grids. The FV summer temperatures are persistently colder than ERA5, whereas the 1° SE grids are not as cold, and are actually warmer than ERA5 at high-latitudes, north of 75° . All grids show a north-south gradient in bias over Greenland, with the summer temperature bias more positive for the northern part of the ice sheet. This pattern is also evident in the near surface temperature bias over Greenland (not shown).

The `Arctic` grid has summer temperatures similar to the 1° SE grids, but is slightly warmer over northern Eurasia and the North Pole (Figure 6). An anomalous cooling patch forms to the west of Greenland, centered over Baffin Island. The `Arctic - GrIS` grid is warmer than the `Arctic` grid over most of the Arctic, but with a similar spatial pattern of summer temperature bias.

Some of these temperature differences may be related to differences in summer cloudiness. Figure 7 shows the summer shortwave cloud forcing bias in the six runs, using the CERES product. Shortwave cloud forcing quantifies the impact of clouds on shortwave radiation, taken as the difference between all-sky and clear-sky shortwave radiative fluxes

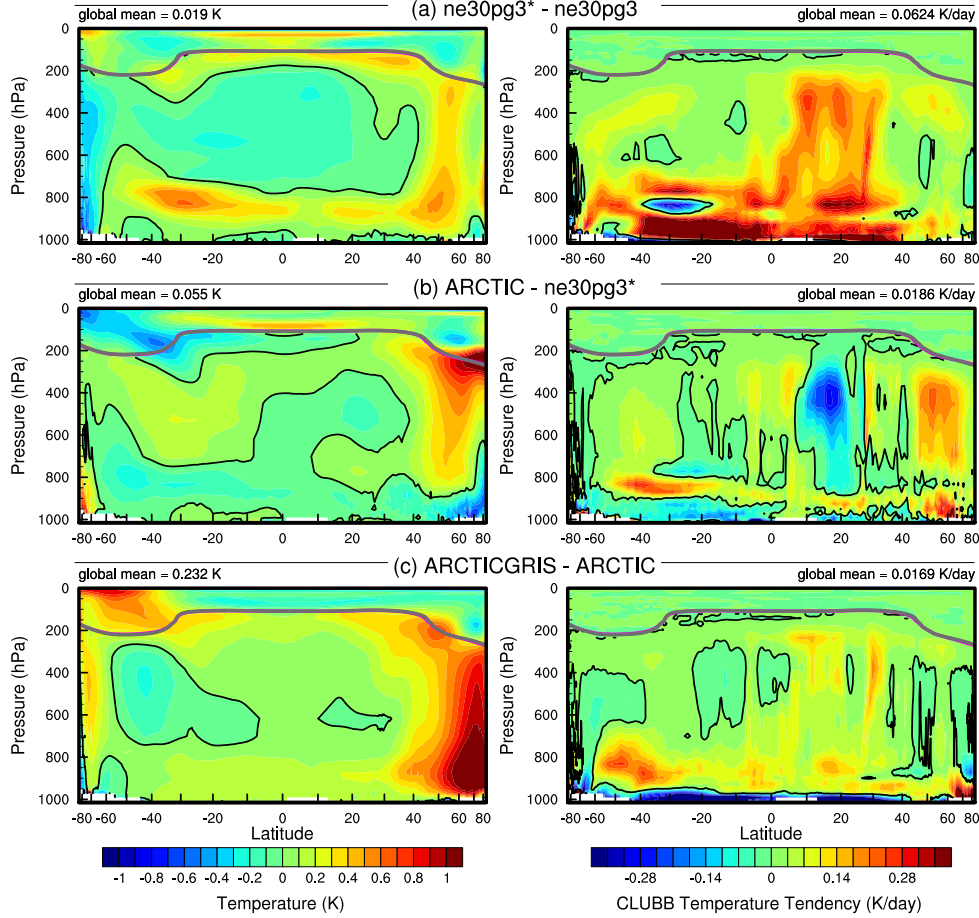


Figure 5. As in Figure 4 but for the short-time-step experiment and the VR grids. The fields plotted are for the climatological northern hemisphere summer. We focus on summer because that is when the resolution response is largest, and the refined regions are located in the northern hemisphere.

535 at the top of the atmosphere. A negative bias corresponds to excessive reflection and cooling.
 536 The lat-lon and quasi-uniform grids have similar biases, with the clouds reflecting
 537 20–40 W/m² too much shortwave radiation over a wide swath of the Arctic, primarily
 538 the land masses. There is also a halo of positive bias (clouds not reflective enough) around
 539 the ocean perimeter of Greenland. The Arctic grid has much smaller cloud forcing bi-
 540 ases over the Arctic land masses, but is still too reflective over Alaska, the Canadian Archipelago,
 541 and parts of Eurasia. Compared to the Arctic grid, the Arctic–GrIS grid vastly re-
 542 duces the cloud forcing bias over Eurasia, and also improves the bias over North Amer-
 543 ica. In both VR grids, the halo of positive shortwave cloud forcing bias around the perime-
 544 ter of Greenland is absent.

545 The summer cloud forcing biases are consistent with the summer temperature bi-
 546 ases in Figure 6 – regions where clouds are too reflective coincide with regions that are
 547 too cold. While we have not quantified the contribution of cloud biases to the cooler Arctic
 548 temperatures, shortwave radiation is a crucial component of the Arctic energy bud-
 549 get during summer. The shortwave cloud forcing biases are on the order of 10 W/m²,
 550 which is a significant fraction of the total absorbed shortwave radiation during Arctic

grid name	accumulation	total melt	runoff	sublimation	SMB
RACMO	681.7 (733.5)	-318.6 (-436.4)	-189.1 (-258.5)	-34.5 (-38.8)	458.1 (436.2)
ne30pg2	1007. (973.4)	-519.9 (-647.3)	-381.9 (-347.0)	-33.9 (-32.1)	591.2 (594.3)
ne30pg3	931.0 (909.3)	-540.8 (-686.7)	-375.8 (-330.1)	-34.1 (-32.6)	521.2 (546.6)
f19	884.9 (913.5)	-414.0 (-546.5)	-284.0 (-284.3)	-36.5 (-37.5)	564.4 (591.7)
f09	873.9 (882.1)	-389.1 (-482.3)	-256.1 (-212.3)	-37.3 (-37.4)	580.5 (632.4)
Arctic	784.1 (818.6)	-335.5 (-436.8)	-215.8 (-194.2)	-42.4 (-43.9)	526.0 (580.5)
Arctic – GrIS	693.8 (747.3)	-437.3 (-610.4)	-276.8 (-307.8)	-48.1 (-51.8)	369.0 (387.7)

Table 3. 1979-1998 surface mass balance of the Greenland Ice Sheet in Gt/yr. Values shown are using the common ice mask approach described in the methods section, whereas values in parentheses are from integrating over the native grid and ice mask.

summer (Serreze et al., 2007) and is therefore likely a factor contributing to the cooler temperatures.

3.2 Clouds and precipitation over Greenland

In addition to summer temperatures, shortwave radiation is an important determinant of snow and ice melt. Figure 8 shows the summer incident shortwave radiation bias at the surface over Greenland and surrounding seas. The top panel shows the bias relative to the RACMO2.3p2 dataset, and the middle panel relative to the CERES dataset. The halo of excessive incident shortwave radiation around the coasts of Greenland is apparent for both datasets in relation to the coarser grids, consistent with the shortwave cloud forcing biases in Figure 7.

The ice sheet interior receives too little shortwave radiation in the coarser grids. On the VR grids, both the interior shortwave deficit and the excessive shortwave around the ocean perimeter are improved. This suggests that the coarse grid clouds are too thick in the interior of Greenland and too thin around the perimeter, which is consistent with the total summer cloud fraction bias, computed from the CALIPSO cloud dataset and shown in the bottom panel of Figure 8. Note that total cloud fraction characterizes the cloud field at all vertical levels, and attenuates the changes arising from any single layer due to the occurrence of overlapping clouds at other levels. The VR grids exhibit an overall improvement in total cloud fraction bias, relative to the coarse grids.

The top panel of Figure 9 shows the annual climatological mean precipitation bias over the GrIS, expressed as the fractional difference from the RACMO2.3p2 solution. The coarse $1^\circ - 2^\circ$ grids have large, positive biases centered over the southern dome. The Arctic grid reduces this bias substantially, and the Arctic–GrIS grid reduces it further, with precipitation centers migrating from the interior toward the margins.

The more accurate representation of orographic precipitation in the VR grids is consistent with the cloud and radiation biases, cf. Figures 7, 8, and 9. The agreement of the cloud, radiation and precipitation biases in and around Greenland from multiple independent datasets indicates that the biases are a robust feature of the coarser grids. The reduced biases in the VR grids suggest that the deficiencies of the coarse grids are due to insufficient horizontal resolution, consistent with previous findings that coarse GCMs have large, positive precipitation biases over Greenland (Pollard & Groups, 2000; Van Kamphout et al., 2019).

3.3 Greenland surface mass balance

Table 3 shows the 1979-1998 climatological SMB components for each grid, compared with RACMO. The values in the table are averages over the ensemble of mapping

methods to the common ice masks described in section 2.7, and the RACMO values refer to the average of both RACMO ensembles. Table 3 also contains (in parenthesis) the SMB components derived from evaluating the integrals on each model’s native grid and ice mask. Of note is the large reduction in melt rates compared to the values computed on the native grid, illustrating the dissipation of this quantity discussed in section 2.7. For integrated precipitation, the differences between the native and common ice mask approaches are much smaller, since the combined solid/liquid precipitation rates are not directly tied to the ice mask.

The coarse grids are characterized by too much precipitation and too much melting and runoff, compared with RACMO. The total SMB on coarse grids therefore has smaller errors than the individual components (Table 3), because large errors in the source and sink terms offset one another when added together. Such compensating errors underline the importance of understanding the extent to which a model is getting the right SMB for the right reasons.

Figure 10 shows time series of annually integrated precipitation and snow/ice melt over the GrIS for the various different grids and dycores, and RACMO in black. The 1979–1998 climatological mean values from Table 3 are shown as circles on the right side of the panels. The 1° – 2° lat-lon and quasi-uniform grids have positive precipitation biases, whereas the VR grids have the smallest biases, with precipitation comparable to RACMO. The f19 and f09 grids perform similarly, with +110 Gt/yr bias, whereas ne30pg3 is biased by about +165 Gt/yr and ne30pg2 by +230 Gt/yr.

The combined annual snow/ice melt shown in the bottom panel of Figure 10 indicates that the Arctic grid simulates the most realistic melt rates, with the other grids having more melt than RACMO. The Arctic–GrIS grid over-predicts melting by about 125 Gt/yr. This is likely due to an anomalously warm lower troposphere during the summer, relative to the Arctic run (Figure 6). The f19 and f09 melting rates are improved over Arctic–GrIS, overestimating melt by only 70–90 Gt/yr. The SE grids have the largest positive melt bias, between 200–220 Gt/yr.

To illustrate the regional behavior of the SMB components, Figure 11 shows the precipitation and combined snow/ice melt integrated over the basins defined by Rignot and Mouginot (2012). The uncertainty due to differences in basin area is larger than for GrIS-wide integrals, owing to the differences in basin boundaries on the common ice masks, which are shown in the f19 and ne30pg2 panels of Figure 9. Nonetheless, the regional totals in Figure 11 correctly show the southeast and southwest basins have the most accumulation. In all basins, accumulation decreases monotonically with increasing grid resolution, though with some exceptions. The Arctic–GrIS grid simulates less precipitation than RACMO in the central-east and southeast basins, and is closest of all grids to RACMO in the large southwest basin.

The basin-integrated melt rates in Figure 11 depend on the dycore. The quasi-uniform SE grids have the largest positive biases in all basins. The Arctic–GrIS grid is a close second, while the FV grids have systematically smaller melt-rates and melt-rate biases. The “second-place” standing of Arctic–GrIS is somewhat unexpected, as this grid has the warmest lower-troposphere summer temperatures (Figure 6) and greatest incident shortwave radiation (Figure 8), yet it has less melting than the quasi-uniform SE grids.

Lower troposphere temperature is not a strict proxy for melting; e.g., it may not capture microclimate effects as a result of a better representation of the low-elevation ablation zones. The Positive Degree-Day temperature-based melt index (PDD; Braithwaite, 1984), which accumulates the near-surface temperature in $^{\circ}\text{C}$ for days with temperature above freezing, is a more accurate proxy for melting. PDD is nonlinear in mean monthly temperature (Reeh, 1991). We compute PDD from monthly mean 2-meter temperature using the method of Calov and Greve (2005), assuming a fixed monthly mean

637 standard deviation of 3°C and a degree-day factor of $5 \text{ mm d}^{-1} ^{\circ}\text{C}^{-1}$. This specific degree-
 638 day factor lies between typical values reported for snow and ice, in order to easily ap-
 639 ply the PDD method to estimate the combined snow and ice melt.

640 Figure 11c shows the basin-integrated PDD melt estimate. In the large southeast
 641 and southwest basins (and all the other western basins), the ne30pg3 grid has larger PDD-
 642 based melt than the Arctic–GrIS grid. The FV grids also have large PDD-based melt
 643 in the southwest basin, relative to Arctic–GrIS. The PDD plots indicate that the re-
 644 lationship between temperature and melt is not well approximated by the summer lower-
 645 troposphere temperatures in Figure 6.

646 The bottom panel of Figure 9 presents the biases in the combined ice/snow melt
 647 as map plots. These plots show that the largest melt biases are on the southeast and north-
 648 west coasts, where large coarse-grid cells overlap with the ocean. One possibility is that
 649 these problematic grid cells are situated at lower elevations than the true ice sheet sur-
 650 face, leading to a warm bias and too much melt. Figure 12 shows the representation of
 651 the ice sheet surface along two transects on the different grids, compared to the high-
 652 resolution dataset used to generate CAM topographic boundary conditions (J. Daniel-
 653 son & Gesch, 2011; Lauritzen et al., 2015). The two transects are shown in Figure 9: the
 654 east-west “K-transect” in southwest Greenland and a transect extending from the cen-
 655 tral dome down to the Kangerlussuaq glacier on the southeast coast. The 1° – 2° grids
 656 are noticeably coarse, with only a handful of grid cells populating the transect. The f09
 657 grid is a bit of an exception since the grid cells narrow in the zonal direction at high lat-
 658 itudes, and so a larger number of grid cells fit into the east-west transects. The VR grids
 659 more accurately reproduce the steep margins of the ice sheet, capturing the character-
 660 istic parabolic shape of the GrIS margin.

661 The transects in Figure 12 show that the ice sheet surface on the coarse grids is
 662 not systematically lower than the true surface in ablation zones. Rather, the smooth-
 663 ing and flattening of the raw topography, necessary to prevent the model from exciting
 664 grid-scale numerical modes, causes the lower-elevation ablation zones to extend beyond
 665 the true ice sheet margin, causing the modeled ablation zones (which must reside within
 666 the ice sheet mask) to be elevated relative to the actual ice surface. The f19 grid has
 667 both the smoothest topography and the flattest ice sheet since its dynamics are coars-
 668 est, whereas the f09, ne30pg2 and ne30pg3 grids have similar dynamical resolution and
 669 use identical smoothing. This suggests that coarser models will tend to elevate the ab-
 670 lation zones relative to where they should be, which may be expected to cause anom-
 671 alous (adiabatic) cooling and depressed melt rates, but this is opposite the melt bias that
 672 occurs in the coarse grid simulations. Also, the EC downscaling should be able to cor-
 673 rect for situations where model ice surface is elevated relative to the true ice surface, al-
 674 though for very large elevation differences/errors the EC scheme may not be adequate.

675 Figure 12 also shows the ice margin boundary, illustrating that the ablation zone
 676 lies in a narrow horizontal band where the ice sheet rapidly plunges to sea-level. Due to
 677 this abrupt transition, coarse grids will commonly represent the ablation zone with grid
 678 cells containing mixtures of ice-covered and ice-free regions. We hypothesize that coarser
 679 models have larger melt biases because summer melting is confined to these mixed ice/land/ocean
 680 grid cells. CLM deals with land heterogeneity in a complex and sophisticated manner,
 681 but CAM only sees the homogenized state after area averaging over the sub-grid mix-
 682 ture. Thus, warm ice-free land patches in a grid cell may unduly influence the climate
 683 over the entire grid cell, causing a warm bias over the ice-covered patch and more melt-
 684 ing.

685 Figure 13 shows the mean melt bias, relative to both RACMO datasets, condition-
 686 ally sampled based on grid cell ice fraction in the GrIS region. Errors are computed af-
 687 ter mapping the melt rates to the common ice masks using different methods, described
 688 in section 2.7. The grid cell ice fractions therefore pertain to ice fractions on the low-

resolution common ice masks. Also shown are the ± 1 standard deviation of the biases for each bin. The figure shows that coarser grids can be characterized by a monotonic increase in melt bias as the grid cell ice fraction decreases. The VR grids have the smallest melt biases for small grid cell ice fractions (less than 50%), the quasi-uniform SE grids and f19 have the largest melt biases and the f09 grid melt biases lie between these two cases. Figure 13 generally supports our hypothesis that the prevalence of mixed-grid cells in the ablation zone of coarse grids is responsible for their large melt bias.

Another potential factor in explaining the melt differences across the grids and dycores is the surface albedo. Bare ice has a lower albedo than snow, so it's reasonable to speculate whether the large melt biases in the coarse grid simulations are in part due to more frequent bare ice exposure. One reasonable pathway to more bare ice exposure is related to the precipitation and cloud biases. As the lat-lon and quasi-uniform grids accumulate too much precipitation in the GrIS interior, it's possible the coastal ice margins receive too little snow, which may be more easily melted away to expose the underlying glacial ice. The top row of Figure 14 shows the summer snow cover bias relative to ERA5. There is no indication that the coastal regions have lower snow fractions, and more bare ice exposure, compared with the VR runs. In southeast Greenland, the coarse runs have anomalously high snow cover relative to the VR runs. In southwest and central-west Greenland, the snow cover is anomalously low, but arguably no more so than occurs in the VR runs. And in combining these results with the precipitation biases (Figure 13), there just isn't much support for a reduction in snowfall and snow cover around the coastal margins in the coarser runs.

The middle and bottom rows of Figure 14 show maps of summer albedo biases in the simulations, relative to the RACMO2.3p2 and the processed MODIS albedo dataset of Tedesco and Alexander (2013). The model surface albedo is diagnosed from the incident and net shortwave radiative fluxes at the surface. While RACMO2.3p2 indicates that the albedo near the southwest/southeast coastal margins is lower in the lat-lon and quasi-uniform grids relative to the VR grids, the MODIS dataset does not show that the VR grids have a substantially different albedo from the coarse grids. We do observe a persistent positive albedo bias in the northwest in all grids, in both validation datasets, which is consistent with a low melt bias in that region (Lofverstrom et al., 2020).

3.4 Precipitation extremes

Synoptic storms are tracked using TempestExtremes atmospheric feature detection software (Ullrich et al., 2021). As the Arctic grid contains $1/4^\circ$ refinement north of about 45° latitude, the storm tracker is applied to this region for the Arctic and ne30pg3 runs to identify differences in storm characteristics due to horizontal resolution.

Figure 15 shows monthly PDF (probability density function) of the precipitation rates associated with storms. The PDFs are constructed by sampling all the precipitation rates within 30° of the storm center, for each point on the storm track and for all storms. The PDFs are evaluated on an identical composite grid for all runs, and so storm statistics are not impacted by differences in output resolution. The Arctic run has larger extreme precipitation rates compared to ne30pg3 in every month, but the increase is greatest in the summer months, which coincides with the most extreme events of the year. This is primarily due to increased resolution and not the reduced physics time step; the ne30pg3* run only marginally increases the extreme precipitation rates compared with ne30pg3 (Figure 15).

The extreme precipitation rates in the Arctic run are closer than ne30pg3 to the ERA5 reanalysis (Figure 15). It is difficult to know how much the extreme precipitation rates in ERA5 are constrained by data assimilation, or whether these precipitation rates are due to using a similar $1/4^\circ$ model as the Arctic grid. However, it is well documented that $1/4^\circ$ models are more skillful at simulating extreme events (Bacmeister et al., 2013;

740 Obrien et al., 2016). A more realistic representation of extreme precipitation events is
 741 an additional benefit of the VR grids.

742 4 Conclusions

743 Running CESM2.2 in an AMIP-style configuration, we have evaluated six grids from
 744 two dynamical cores for their performance over the Arctic and in simulating the GrIS
 745 SMB. The $1 - 2^\circ$ finite-volume grids have enhanced resolution over polar regions due
 746 to their convergence of meridian lines, although a polar filter is used to prevent spuri-
 747 ous atmospheric features from forming in these regions. SE grids comparable to the res-
 748 olution of the FV grids have an isotropic grid structure where the grid resolution is sim-
 749 ilar over the entire model domain. We developed two VR grids and introduced them into
 750 CESM2.2 as part of this work. Both use the SE dycore; the **Arctic** grid has $1/4^\circ$ refine-
 751 ment over the broader Arctic, whereas the **Arctic – GrIS** grid is identical except for
 752 a $1/8^\circ$ patch of refinement over Greenland. A third VR grid, **CONUS**, with $1/8^\circ$ refine-
 753 ment over the US, has also been made available in CESM2.2.

754 In general, the FV grids have colder summer temperatures over the Arctic com-
 755 pared with the SE grids (including the VR grids). The cloud biases in all the **lat-lon and**
 756 **quasi-uniform** resolution grids, whether FV or SE, are similar, in general being too cloudy
 757 over Arctic land masses. It should be emphasized that our analysis is specific to the Arc-
 758 tic summer because of its relevance to GrIS melt rates. An improved representation of
 759 clouds in the Arctic does not imply improved clouds at lower latitudes.

760 At the regional level, there is a halo of negative cloudiness bias around the ocean
 761 perimeter of Greenland on all $1 - 2^\circ$ grids, but not the VR grids. This negative cloud
 762 bias contrasts with a positive cloud bias over the ice sheet interior. This anomaly pat-
 763 tern is attributed to deficient orographic precipitation in the coarser model grids. With
 764 overly smooth topography on the $1 - 2^\circ$ grids, synoptic systems moving into Greenland
 765 are not sufficiently lifted when encountering the steep ice margins. As a result, excess
 766 precipitation falls in the GrIS interior, instead of being concentrated on the steep coastal
 767 margins as shown by observations (Pollard & Groups, 2000; Van Kampenhout et al., 2019).
 768 This results in a positive precipitation and cloud bias in the ice sheet interior, and a halo
 769 of low cloud bias about the perimeter. The agreement of different observational data prod-
 770 ucts on this bias lends confidence in the attribution of causes. The VR grids compare
 771 better to the observations and show that orographic precipitation in Greenland is largely
 772 resolved when the horizontal resolution is increased sufficiently.

773 We integrated the primary source and sink terms of the SMB equation over the GrIS
 774 for each of the six grids. The **1° – 2° lat-lon and quasi-uniform** grids have large posi-
 775 tive accumulation biases because they fail to resolve orographic precipitation. The quasi-
 776 uniform SE grids have larger accumulation biases, suggesting that the FV grids are more
 777 skillful for precipitation due to finer resolution over Greenland, and despite a polar fil-
 778 ter. The VR grids have the most accurate accumulation rates of all the grids. The pri-
 779 mary mass sink term of the GrIS, ice/snow melt, has similar biases; the coarse grids melt
 780 too much, with a greater bias for quasi-uniform SE grids. In general, on coarse grids, er-
 781 rors in the individual SMB terms are larger than the errors in the SMB itself, due to com-
 782 pensating errors. This observation serves as a precaution; projecting mass-loss from a
 783 glacier or ice sheet cannot be reliable if the processes representing the components of the
 784 SMB are incorrect from the start, even if the total SMB has the right magnitude.

785 The **Arctic – GrIS** grid has the warmest summer lower troposphere of all grids,
 786 yet it has less melting than the quasi-uniform resolution SE grids. This suggests that
 787 grid resolution is somehow contributing to the melt biases in coarse grids, in a way that
 788 is not obvious from the large-scale dynamics. We propose a mechanism: coarse grids rep-
 789 resent ablation zones using grid cells with mixed surface types, ice-covered and ice-free.

790 The warmer ice-free patches may largely determine the mean state, leading to a warm
 791 bias over the ice-covered patches of the grid cell. This mechanism is supported by anal-
 792 ysis of melt biases binned by grid-cell ice fraction, although further testing of this hy-
 793 pothesis is needed.

794 The **Arctic** grid substantially improves the simulated Arctic climate, including pre-
 795 cipitation extremes and the GrIS SMB, compared to the **1°–2° lat-lon and quasi-uniform**
 796 grids. The **Arctic–GrIS** grid has the most realistic cloud and precipitation fields, but
 797 its summer temperatures are too warm. The **1° FV** model gives a surprisingly realistic
 798 SMB, likely due to the relatively fine resolution of Greenland on lat-lon grids (but per-
 799 haps also because it is the most heavily tuned model configuration in CESM). In par-
 800 ticular, a greater number of grid cells in the ablation zone reduces the influence of mixed
 801 ice-covered/ice-free grid cells that represent ablation poorly on the other **lat-lon and quasi-**
 802 uniform grids.

803 As modeling systems move away from lat-lon grids towards quasi-uniform unstruc-
 804 tured grids, it is worth taking stock of whether this will degrade the simulated polar cli-
 805 mate. We have found that the **1° FV** model has clear advantages over the **1° SE** model
 806 for simulating the GrIS SMB. The **SE dycore is still under active development** (e.g., Ap-
 807 pendix A) compared to the more mature **FV dycore**, and future algorithmic improve-
 808 ments may reduce the **FV-SE GrIS SMB skill gap**. However, such developments are un-
 809 likely to eliminate this skill gap entirely due to the fewer number of grid cells represent-
 810 ing high latitude structures on quasi-uniform unstructured grids. The simulated GrIS
 811 SMB will be adversely impacted in future CESM versions, after the **FV dycore** is phased
 812 out. This finding will not interrupt the ongoing transition towards unstructured grids
 813 in CESM, which is largely driven by gains in computational efficiency and grid refine-
 814 ment capabilities. We therefore provide the Arctic refined-meshes to the community by
 815 way of CESM2.2, providing users the option to simulate a more realistic GrIS SMB, al-
 816 though at a substantial computational premium relative to conventional **1°–2°** grids.

817 We are working to develop a configuration of the **Arctic** grid that is fully-coupled
 818 with the CESM ocean and sea ice components and the Community Ice Sheet Model (CISM),
 819 to provide multi-century projections of the state of the GrIS and its contribution to sea-
 820 level rise. We have also developed a visualization of the **Arctic–GrIS** run, now avail-
 821 able on youtube (see link in Acknowledgements) to increase awareness of the capabil-
 822 ities of CESM2.2. Figure 16 shows a snapshot of this visualization, illustrating mesoscale
 823 katabatic winds descending the southeastern slopes of the GrIS. These new grids and con-
 824 figurations will provide new opportunities for CESM polar science, and they aim to con-
 825 tribute to an improved understanding of the polar environment. However, we recognize
 826 the potentially prohibitive costs for some users, and so will continue to explore differ-
 827 ent grids, parameterizations and workflows that can provide some of the same benefits
 828 of the VR grids, but at a lower cost.

829 **Appendix A Details on spectral-element dynamical core improvements** 830 **since the CESM2.0 release**

831 Since the CESM2.0 release of the spectral-element dynamical core documented in
 832 Lauritzen et al. (2018) some important algorithmic improvements have been implemented
 833 and released with CESM2.2. These pertain mainly to the flow over orography that, for
 834 the spectral-element dynamical core, can lead to noise aligned with the element bound-
 835 aries (Herrington et al., 2018).

836 **A1 Reference profiles**

837 Significant improvement in removing noise for flow over orography can be achieved
 838 by using reference profiles for temperature and pressure

$$T^{(ref)} = T_0 + T_1 \Pi^{(ref)}, \quad (\text{A1})$$

$$p_s^{(ref)} = p_0 \exp\left(-\frac{\Phi_s}{R^{(d)} T_{ref}}\right), \quad (\text{A2})$$

839 (Simmons & Jiabin, 1991) where $T_1 = \Gamma_0 T_{ref} c_p^{(d)} / g \approx 192K$, with gravity \mathbf{g} , and stan-
 840 dard lapse rate $\Gamma_0 \equiv 6.5K/km$ and $T_0 \equiv T_{ref} - T_1 \approx 97K$; $T_{ref} = 288K$ ($c_p^{(d)}$ specific
 841 heat of dry air at constant pressure; $R^{(d)}$ gas constant for dry air), and Φ_s is the sur-
 842 face geopotential. The reference Exner function is

$$\Pi^{(ref)} = \left(\frac{p^{(ref)}}{p_0}\right)^\kappa \quad (\text{A3})$$

843 where $\kappa = \frac{R^{(d)}}{c_p^{(d)}}$. The reference surface pressure $p_0 = 1000hPa$ and at each model level
 844 the reference pressure $p^{(ref)}$ is computed from $p_s^{(ref)}$ and the standard hybrid coefficients

$$p^{(ref)}(\eta) = A(\eta)p_0 + B(\eta)p_s^{(ref)}, \quad (\text{A4})$$

845 where A and B are the standard hybrid coefficients (using a dry-mass generalized ver-
 846 tical mass coordinate η). These reference profiles are subtracted from the prognostic tem-
 847 perature and pressure-level-thickness states before applying hyperviscosity:

CESM2.0 → CESM2.2

$$\nabla_\eta^4 T \rightarrow \nabla_\eta^4 (T - T^{(ref)}), \quad (\text{A5})$$

$$\nabla_\eta^4 \delta p^{(d)} \rightarrow \nabla_\eta^4 (\delta p^{(d)} - \delta p^{(ref)}). \quad (\text{A6})$$

848 This reduces spurious transport of temperature and mass up/down-slope due to the hy-
 849 perviscosity operator.

850 **A2 Rewriting the pressure gradient force (PGF)**

851 In the CESM2.0 the following (standard) form of the pressure gradient term was
 852 used:

$$\nabla_\eta \Phi + \frac{1}{\rho} \nabla_\eta p, \quad (\text{A7})$$

853 where Φ is geopotential and $\rho = \frac{R^{(d)} T_v}{p}$ is density (for details see Lauritzen et al., 2018).
 854 To alleviate noise for flow over orography, we switched to an Exner pressure formulation
 855 following Taylor et al. (2020), which uses that (A7) can be written in terms of the Exner
 856 pressure

$$\nabla_\eta \Phi + c_p^{(d)} \theta_v \nabla_\eta \Pi, \quad (\text{A8})$$

857 where the Exner pressure is

$$\Pi \equiv \left(\frac{p}{p_0}\right)^\kappa. \quad (\text{A9})$$

858 and virtual temperature is

$$T_v = T \left(\frac{1 + \frac{1}{\epsilon} m^{(wv)}}{\sum_{\ell \in \mathcal{L}_{all}} m^{(\ell)}} \right), \quad (\text{A10})$$

859 where $m^{(\ell)}$ is dry mixing ratio of component of moist air ℓ ; \mathcal{L}_{all} is the set of all compo-
 860 nents of moist air and, in particular, ' wv ' is water vapor.

The derivation showing that (A7) and (A8) are equivalent is given here:

$$\begin{aligned}
c_p^{(d)} \theta_v \nabla_\eta \Pi &= c_p^{(d)} \theta_v \nabla_\eta \left(\frac{p}{p_0} \right)^\kappa, \\
&= c_p^{(d)} \theta_v \kappa \left(\frac{p}{p_0} \right)^{\kappa-1} \nabla_\eta \left(\frac{p}{p_0} \right), \\
&= c_p^{(d)} \theta_v \kappa \Pi \left(\frac{p_0}{p} \right) \nabla_\eta \left(\frac{p}{p_0} \right), \\
&= \frac{c_p^{(d)} \theta_v \kappa \Pi}{p} \nabla_\eta p, \\
&= \frac{R^{(d)} \theta_v \Pi}{p} \nabla_\eta p, \\
&= \frac{R^{(d)} T_v}{p} \nabla_\eta p, \\
&= \frac{1}{\rho} \nabla_\eta p.
\end{aligned}$$

where virtual potential temperature is T_v/Π . Using the reference states from (Simmons & Jiabin, 1991),

$$\bar{T} = T_0 + T_1 \Pi, \quad (\text{A11})$$

$$\bar{\theta} = T_0/\Pi + T_1, \quad (\text{A12})$$

we can define a geopotential as a function of Exner pressure

$$\bar{\Phi} = -c_p^{(d)} (T_0 \log \Pi + T_1 \Pi - T_1). \quad (\text{A13})$$

This "balanced" geopotential obeys

$$c_p^{(d)} \bar{\theta} \nabla \Pi + \nabla \bar{\Phi} = 0 \quad (\text{A14})$$

for any Exner pressure. Subtracting this "reference" profile from the PGF yields

$$\begin{aligned}
\nabla_\eta \Phi + c_p^{(d)} \theta_v \nabla_\eta \Pi &= \nabla_\eta (\Phi - \bar{\Phi}) + c_p^{(d)} (\theta_v - \bar{\theta}) \nabla_\eta \Pi, \\
&= \nabla_\eta \Phi + c_p^{(d)} \theta_v \nabla_\eta \Pi + c_p^{(d)} T_0 \left[\nabla_\eta \log \Pi - \frac{1}{\Pi} \nabla_\eta \Pi \right]. \quad (\text{A15})
\end{aligned}$$

In the continuum, the two formulations (left and right-hand side of (A15)) are identical. But under discretization, the second formulation can have much less truncation error.

A3 Results

One year averages of vertical pressure velocity at 500hPa (OMEGA500) have been found to be a useful quantity to detect spurious up or down-drafts induced by steep orography (Figure A1). While the true solution is not known, strong vertical velocities aligned with element edges that are not found in the CAM-FV reference solution (Figure A1(a)) are likely not physical (spurious). The older CESM2.0 version of SE (Figure A1(d)) using the "traditional" discretization of the PGF, (A15), exhibits significant spurious noise patterns around steep orography compared to CAM-FV (e.g., around Himalayas and Andes). This is strongly alleviated by switching to the Exner formulation of the PGF (A8; Figure A1(c)). By also subtracting reference profiles from pressure-level thickness and temperature, equations (A5) and (A6) respectively, reduces strong up-down drafts further (Figure A1(d)). Switching to the CAM-SE-CSLAM version where physics tendencies are computed on an quasi-equal area physics grid and using the CSLAM transport scheme, marginal improvements are observed in terms of a smoother vertical velocity field

(Figure A1(e,f)). The configuration shown in Figure A1(d) is used for the simulations shown in the main text of this paper.

It is interesting to note that the noise issues and algorithmic remedies found in the real-world simulations discussed above, can be investigated by replacing all of physics with a modified version of the Held-Suarez forcing (Held & Suarez, 1994). The original formulation of the Held-Suarez idealized test case used a flat Earth ($\Phi_s = 0$) and a dry atmosphere. By simply adding the surface topography used in ‘real-world’ simulations and removing the temperature relaxation in the lower part of domain ($\sigma > 0.7$; see Held and Suarez (1994) for details), surprisingly realistic vertical velocity fields (in terms of structure) result (see Figure A2). Since this was a very useful development tool it is shared in this manuscript.

Acknowledgments

This material is based upon work supported by the National Center for Atmospheric Research (NCAR), which is a major facility sponsored by the NSF under Cooperative Agreement 1852977. Computing and data storage resources, including the Cheyenne supercomputer (Computational and Information Systems Laboratory, 2017), were provided by the Computational and Information Systems Laboratory (CISL) at NCAR. A. Herrington thanks Matt Rehme (NCAR/CISL) for his role in generating the Arctic–GrIS visualization available on youtube (https://www.youtube.com/watch?v=YwHgqDu75s8&t=4s&ab_channel=NCARVisLab).

The data presented in main part of this manuscript is available at <https://github.com/adamrher/2020-arcticgrids>. The source code and data for the Appendix is available at <https://github.com/PeterHjortLauritzen/CAM/tree/topo-mods>.

References

- Alexander, P., LeGrande, A., Fischer, E., Tedesco, M., Fettweis, X., Kelley, M., ...
 Schmidt, G. (2019). Simulated greenland surface mass balance in the giss modele2 gcm: Role of the ice sheet surface. *Journal of Geophysical Research: Earth Surface*, 124(3), 750–765.
- Bacmeister, J. T., Reed, K. A., Hannay, C., Lawrence, P., Bates, S., Truesdale, J. E., ... Levy, M. (2016). Projected changes in tropical cyclone activity under future warming scenarios using a high-resolution climate model. *Climatic Change*. doi: 10.1007/s10584-016-1750-x
- Bacmeister, J. T., Wehner, M. F., Neale, R. B., Gettelman, A., Hannay, C., Lauritzen, P. H., ... Truesdale, J. E. (2013). Exploratory high-resolution climate simulations using the community atmosphere model (cam). *J. Climate*, 27(9), 3073–3099. doi: 10.1175/JCLI-D-13-00387.1
- Bambach, N. E., Rhoades, A. M., Hatchett, B. J., Jones, A. D., Ullrich, P. A., & Zarzycki, C. M. (2021). Projecting climate change in south america using variable-resolution community earth system model: An application to chile. *International Journal of Climatology*.
- Beljaars, A., Brown, A., & Wood, N. (2004). A new parametrization of turbulent orographic form drag. *Quart. J. Roy. Meteor. Soc.*, 130(599), 1327–1347. doi: 10.1256/qj.03.73
- Bogenschutz, P. A., Gettelman, A., Morrison, H., Larson, V. E., Craig, C., & Schanen, D. P. (2013). Higher-order turbulence closure and its impact on climate simulations in the community atmosphere model. *Journal of Climate*, 26(23), 9655–9676.
- Box, J. E., Bromwich, D. H., & Bai, L.-S. (2004). Greenland ice sheet surface mass balance 1991–2000: Application of polar mm5 mesoscale model and in situ data. *Journal of Geophysical Research: Atmospheres*, 109(D16).

- 934 Braithwaite, R. J. (1984). Calculation of degree-days for glacier-climate research.
 935 *Zeitschrift für Gletscherkunde und Glazialgeologie*, 20(1984), 1–8.
- 936 Burakowski, E. A., Tawfik, A., Ouimette, A., Lepine, L., Zarzycki, C., Novick, K.,
 937 ... Bonan, G. (2019). Simulating surface energy fluxes using the variable-
 938 resolution community earth system model (vr-cesm). *Theoretical and Applied
 939 Climatology*, 138(1), 115–133.
- 940 Calov, R., & Greve, R. (2005). A semi-analytical solution for the positive degree-day
 941 model with stochastic temperature variations. *Journal of Glaciology*, 51(172),
 942 173–175.
- 943 Canuto, C., Hussaini, M. Y., Quarteroni, A., & Zang, T. (2007). *Spectral methods:
 944 Evolution to complex geometries and applications to fluid dynamics* (1st ed.).
 945 Springer.
- 946 Chang, P., Zhang, S., Danabasoglu, G., Yeager, S. G., Fu, H., Wang, H., ... oth-
 947 ers (2020). An unprecedented set of high-resolution earth system simulations
 948 for understanding multiscale interactions in climate variability and change.
 949 *Journal of Advances in Modeling Earth Systems*, 12(12), e2020MS002298.
- 950 Chepfer, H., Bony, S., Winker, D., Cesana, G., Dufresne, J., Minnis, P., ... Zeng, S.
 951 (2010). The gcm-oriented calipso cloud product (calipso-goccp). *Journal of
 952 Geophysical Research: Atmospheres*, 115(D4).
- 953 Collins, W. D., Rasch, P. J., Boville, B. A., Hack, J. J., McCaa, J. R., Williamson,
 954 D. L., ... Zhang, M. (2006). The formulation and atmospheric simulation
 955 of the community atmosphere model version 3 (cam3). *Journal of Climate*,
 956 19(11), 2144–2161.
- 957 Computational and Information Systems Laboratory. (2017). *Cheyenne: HPE/SGI
 958 ICE XA System (Climate Simulation Laboratory)*, Boulder, CO: National
 959 Center for Atmospheric Research. doi: 10.5065/D6RX99HX
- 960 Copernicus, C. (2019). Era5 monthly averaged data on pressure levels from
 961 1979 to present. URL: <https://cds.climate.copernicus.eu>. doi: 10.24381/
 962 cds.6860a573
- 963 Craig, C., Bacmeister, J., Callaghan, P., Eaton, B., Gettelman, A., Goldhaber, S. N.,
 964 ... Vitt, F. M. (2021). *Cam6.3 user's guide* (Tech. Rep.). NCAR/TN-
 965 571+EDD. doi: 10.5065/Z953-ZC95
- 966 Danabasoglu, G., Lamarque, J.-F., Bacmeister, J., Bailey, D., DuVivier, A., Ed-
 967 wards, J., ... others (2020). The community earth system model ver-
 968 sion 2 (cesm2). *Journal of Advances in Modeling Earth Systems*, 12(2),
 969 e2019MS001916.
- 970 Danielson, J., & Gesch, D. (2011). *Global multi-resolution terrain elevation data
 971 2010 (GMTED2010)* (Open-File Report 2011-1073). U.S. Geological Survey.
 972 (<http://pubs.usgs.gov/of/2011/1073/pdf/of2011-1073.pdf>)
- 973 Danielson, J. J., & Gesch, D. B. (2011). *Global multi-resolution terrain elevation
 974 data 2010 (GMTED2010)* (Open File Rep. No. 2011-1073). US Geological Sur-
 975 vey. doi: <https://doi.org/10.3133/ofr20111073>
- 976 Dennis, J., Edwards, J., Evans, K. J., Guba, O., Lauritzen, P. H., Mirin, A. A., ...
 977 Worley, P. H. (2012). CAM-SE: A scalable spectral element dynamical core for
 978 the Community Atmosphere Model. *Int. J. High. Perform. C.*, 26(1), 74-89.
 979 Retrieved from <http://hpc.sagepub.com/content/26/1/74.abstract> doi:
 980 10.1177/1094342011428142
- 981 Dennis, J., Fournier, A., Spotz, W., St-Cyr, A., Taylor, M., Thomas, S., & Tufo, H.
 982 (2005). High-resolution mesh convergence properties and parallel efficiency
 983 of a spectral element atmospheric dynamical core. *ijhpc*, 19, 225-235. doi:
 984 10.1177/1094342005056108
- 985 Evans, K. J., Kennedy, J. H., Lu, D., Forrester, M. M., Price, S., Fyke, J., ... oth-
 986 ers (2019). Livvkit 2.1: automated and extensible ice sheet model validation.
 987 *Geoscientific Model Development*, 12(3), 1067–1086.
- 988 Eyring, V., Bony, S., Meehl, G. A., Senior, C. A., Stevens, B., Stouffer, R. J., &

- 989 Taylor, K. E. (2016). Overview of the coupled model intercomparison project
 990 phase 6 (cmip6) experimental design and organization. *Geoscientific Model*
 991 *Development*, 9(5), 1937–1958.
- 992 Fettweis, X., Franco, B., Tedesco, M., Van Angelen, J., Lenaerts, J. T., van den
 993 Broeke, M. R., & Gallée, H. (2013). Estimating the greenland ice sheet
 994 surface mass balance contribution to future sea level rise using the regional
 995 atmospheric climate model mar. *The Cryosphere*, 7(2), 469–489.
- 996 Gettelman, A., Callaghan, P., Larson, V., Zarzycki, C., Bacmeister, J., Lauritzen, P.,
 997 ... Neale, R. (2017). Regional climate simulations with the community earth
 998 system model. *J. Adv. Model. Earth Syst.*. (submitted)
- 999 Gettelman, A., Hannay, C., Bacmeister, J. T., Neale, R. B., Pendergrass, A., Dan-
 1000 abasoglu, G., ... others (2019). High climate sensitivity in the community
 1001 earth system model version 2 (cesm2). *Geophysical Research Letters*, 46(14),
 1002 8329–8337.
- 1003 Gettelman, A., & Morrison, H. (2015). Advanced two-moment bulk microphysics for
 1004 global models. part i: Off-line tests and comparison with other schemes. *Journal*
 1005 *of Climate*, 28(3), 1268–1287.
- 1006 Gettelman, A., Morrison, H., Santos, S., Bogenschutz, P., & Caldwell, P. (2015).
 1007 Advanced two-moment bulk microphysics for global models. part ii: Global
 1008 model solutions and aerosol–cloud interactions. *Journal of Climate*, 28(3),
 1009 1288–1307.
- 1010 Golaz, J.-C., Larson, V. E., & Cotton, W. R. (2002). A pdf-based model for bound-
 1011 ary layer clouds. part i: Method and model description. *Journal of the Atmo-*
 1012 *spheric Sciences*, 59(24), 3540–3551. doi: 10.1175/1520-0469(2002)059<3540:
 1013 apbmfb>2.0.co;2
- 1014 Guba, O., Taylor, M. A., Ullrich, P. A., Overfelt, J. R., & Levy, M. N. (2014). The
 1015 spectral element method (sem) on variable-resolution grids: evaluating grid
 1016 sensitivity and resolution-aware numerical viscosity. *Geosci. Model Dev.*, 7(6),
 1017 2803–2816. doi: 10.5194/gmd-7-2803-2014
- 1018 Guo, Z., Wang, M., Qian, Y., Larson, V. E., Ghan, S., Ovchinnikov, M., ... Zhou,
 1019 T. (2015). Parametric behaviors of clubb in simulations of low clouds in the c
 1020 ommunity atmosphere m odel (cam). *Journal of Advances in Modeling Earth*
 1021 *Systems*, 7(3), 1005–1025.
- 1022 Hansen, N., Simonsen, S. B., Boberg, F., Kittel, C., Orr, A., Souverijns, N., ... Mot-
 1023 tram, R. (2022). Brief communication: Impact of common ice mask in surface
 1024 mass balance estimates over the antarctic ice sheet. *The Cryosphere*, 16(2),
 1025 711–718.
- 1026 Held, I. M., & Suarez, M. J. (1994). A proposal for the intercomparison of the dy-
 1027 namical cores of atmospheric general circulation models. *Bull. Am. Meteorol.*
 1028 *Soc.*, 73, 1825–1830.
- 1029 Herrington, A. R., Lauritzen, P., Taylor, M. A., Goldhaber, S., Eaton, B. E.,
 1030 Bacmeister, J., ... Ullrich, P. (2018). Physics-dynamics coupling with element-
 1031 based high-order galerkin methods: quasi equal-area physics grid. *Mon. Wea.*
 1032 *Rev.*, 47, 69–84. doi: 10.1175/MWR-D-18-0136.1
- 1033 Herrington, A. R., Lauritzen, P. H., Reed, K. A., Goldhaber, S., & Eaton, B. E.
 1034 (2019). Exploring a lower resolution physics grid in cam-se-cslam. *Journal of*
 1035 *Advances in Modeling Earth Systems*, 11.
- 1036 Herrington, A. R., & Reed, K. A. (2018). An idealized test of the response of the
 1037 community atmosphere model to near-grid-scale forcing across hydrostatic
 1038 resolutions. *J. Adv. Model. Earth Syst.*, 10(2), 560–575.
- 1039 Herrington, A. R., & Reed, K. A. (2020). On resolution sensitivity in the commu-
 1040 nity atmosphere model. *Quarterly Journal of the Royal Meteorological Society*,
 1041 146(733), 3789–3807.
- 1042 Hurrell, J. W., Hack, J. J., Shea, D., Caron, J. M., & Rosinski, J. (2008). A new
 1043 sea surface temperature and sea ice boundary dataset for the community at-

- mosphere model. *Journal of Climate*, 21(19), 5145–5153.
- Jablonowski, C., & Williamson, D. L. (2011). The pros and cons of diffusion, filters and fixers in atmospheric general circulation models. In P. H. Lauritzen, C. Jablonowski, M. Taylor, & R. Nair (Eds.), *Numerical techniques for global atmospheric models* (pp. 381–493). Berlin, Heidelberg: Springer Berlin Heidelberg. doi: 10.1007/978-3-642-11640-7_13
- Lauritzen, P. H., Bacmeister, J. T., Callaghan, P. F., & Taylor, M. A. (2015). NCAR_Topo (v1.0): NCAR global model topography generation software for unstructured grids. *Geosci. Model Dev.*, 8(12), 3975–3986. doi: 10.5194/gmd-8-3975-2015
- Lauritzen, P. H., Jablonowski, C., Taylor, M., & Nair, R. D. (2010). Rotated versions of the jablonowski steady-state and baroclinic wave test cases: A dynamical core intercomparison. *J. Adv. Model. Earth Syst.*, 2(15), 34 pp.
- Lauritzen, P. H., Mirin, A., Truesdale, J., Raeder, K., Anderson, J., Bacmeister, J., & Neale, R. B. (2011). Implementation of new diffusion/filtering operators in the CAM-FV dynamical core. *Int. J. High Perform. Comput. Appl.*. doi: 10.1177/1094342011410088
- Lauritzen, P. H., Nair, R., Herrington, A., Callaghan, P., Goldhaber, S., Dennis, J., ... Dubos, T. (2018). NCAR release of CAM-SE in CESM2.0: A reformulation of the spectral-element dynamical core in dry-mass vertical coordinates with comprehensive treatment of condensates and energy. *J. Adv. Model. Earth Syst.*, 10(7), 1537–1570. doi: 10.1029/2017MS001257
- Lauritzen, P. H., Taylor, M. A., Overfelt, J., Ullrich, P. A., Nair, R. D., Goldhaber, S., & Kelly, R. (2017). CAM-SE-CSLAM: Consistent coupling of a conservative semi-lagrangian finite-volume method with spectral element dynamics. *Mon. Wea. Rev.*, 145(3), 833–855. doi: 10.1175/MWR-D-16-0258.1
- Lawrence, D. M., Fisher, R. A., Koven, C. D., Oleson, K. W., Swenson, S. C., Bonan, G., ... others (2019). The community land model version 5: Description of new features, benchmarking, and impact of forcing uncertainty. *Journal of Advances in Modeling Earth Systems*, 11(12), 4245–4287.
- Lin, S.-J. (2004). A 'vertically Lagrangian' finite-volume dynamical core for global models. *Mon. Wea. Rev.*, 132, 2293–2307.
- Lin, S.-J., & Rood, R. B. (1997). An explicit flux-form semi-Lagrangian shallow-water model on the sphere. *Q.J.R. Meteorol. Soc.*, 123, 2477–2498.
- Lipscomb, W. H., Fyke, J. G., Vizcaíno, M., Sacks, W. J., Wolfe, J., Vertenstein, M., ... Lawrence, D. M. (2013). Implementation and initial evaluation of the glimmer community ice sheet model in the community earth system model. *Journal of Climate*, 26(19), 7352–7371.
- Loeb, N. G., Doelling, D. R., Wang, H., Su, W., Nguyen, C., Corbett, J. G., ... Kato, S. (2018). Clouds and the earth's radiant energy system (ceres) energy balanced and filled (ebaf) top-of-atmosphere (toa) edition-4.0 data product. *Journal of Climate*, 31(2), 895–918.
- Lofverstrom, M., Fyke, J. G., Thayer-Calder, K., Muntjewerf, L., Vizcaino, M., Sacks, W. J., ... Bradley, S. L. (2020). An efficient ice sheet/earth system model spin-up procedure for csm2-cism2: Description, evaluation, and broader applicability. *Journal of Advances in Modeling Earth Systems*, 12(8), e2019MS001984.
- Morlighem, M., Rignot, E., Mouginot, J., Seroussi, H., & Larour, E. (2014). Deeply incised submarine glacial valleys beneath the greenland ice sheet. *Nature Geoscience*, 7(6), 418–422.
- Mottram, R., Boberg, F., Langen, P., Yang, S., Rodehacke, C., Christensen, J. H., & Madsen, M. S. (2017). Surface mass balance of the greenland ice sheet in the regional climate model hirham5: Present state and future prospects. *Low Temp. Sci.*, 75, 105–115.
- Muntjewerf, L., Sacks, W. J., Lofverstrom, M., Fyke, J., Lipscomb, W. H., Er-

- nani da Silva, C., ... Sellevold, R. (2021). Description and Demonstration of the Coupled Community Earth System Model v2–Community Ice Sheet Model v2 (CESM2-CISM2). *Journal of Advances in Modeling Earth Systems*, 13(6), e2020MS002356.
- Neale, R. B., Richter, J. H., & Jochum, M. (2008). The impact of convection on ENSO: From a delayed oscillator to a series of events. *J. Climate*, 21, 5904-5924.
- Noël, B., Van De Berg, W., Van Meijgaard, E., Kuipers Munneke, P., Van De Wal, R., & Van Den Broeke, M. (2015). Evaluation of the updated regional climate model racmo2. 3: summer snowfall impact on the greenland ice sheet. *The Cryosphere*, 9(5), 1831–1844.
- Noël, B., van de Berg, W. J., Lhermitte, S., & van den Broeke, M. R. (2019). Rapid ablation zone expansion amplifies north greenland mass loss. *Science advances*, 5(9), eaaw0123.
- Noël, B., van de Berg, W. J., Van Wessem, J. M., Van Meijgaard, E., Van As, D., Lenaerts, J., ... others (2018). Modelling the climate and surface mass balance of polar ice sheets using racmo2–part 1: Greenland (1958–2016). *The Cryosphere*, 12(3), 811–831.
- Obrien, T. A., Collins, W. D., Kashinath, K., Rübel, O., Byna, S., Gu, J., ... Ullrich, P. A. (2016). Resolution dependence of precipitation statistical fidelity in hindcast simulations. *J. Adv. Model. Earth Syst.*, 8(2), 976–990. Retrieved from <http://dx.doi.org/10.1002/2016ms000671> doi: 10.1002/2016ms000671
- Ohmura, A. (2001). Physical basis for the temperature-based melt-index method. *Journal of applied Meteorology*, 40(4), 753–761.
- Pfister, G. G., Eastham, S. D., Arellano, A. F., Aumont, B., Barsanti, K. C., Barth, M. C., ... others (2020). The multi-scale infrastructure for chemistry and aerosols (musica). *Bulletin of the American Meteorological Society*, 101(10), E1743–E1760.
- Pollard, D. (2010). A retrospective look at coupled ice sheet–climate modeling. *Climatic Change*, 100(1), 173–194.
- Pollard, D., & Groups, P. P. (2000). Comparisons of ice-sheet surface mass budgets from paleoclimate modeling intercomparison project (pmip) simulations. *Global and Planetary Change*, 24(2), 79–106.
- Pope, V., & Stratton, R. (2002). The processes governing horizontal resolution sensitivity in a climate model. *Climate Dynamics*, 19(3-4), 211–236.
- Putman, W. M., & Lin, S.-J. (2007). Finite-volume transport on various cubed-sphere grids. *J. Comput. Phys.*, 227(1), 55–78.
- Rae, J., Adalgeirsdóttir, G., Edwards, T. L., Fettweis, X., Gregory, J., Hewitt, H., ... others (2012). Greenland ice sheet surface mass balance: evaluating simulations and making projections with regional climate models. *The Cryosphere*, 6(6), 1275–1294.
- Rasch, P. J., & Williamson, D. L. (1990). Computational aspects of moisture transport in global models of the atmosphere. *Q. J. R. Meteorol. Soc.*, 116, 1071–1090.
- Reeh, N. (1991). Parameterization of melt rate and surface temperature in the greenland ice sheet. *Polarforschung*, 59(3), 113–128.
- Rhoades, A. M., Huang, X., Ullrich, P. A., & Zarzycki, C. M. (2016). Characterizing sierra nevada snowpack using variable-resolution cesm. *Journal of Applied Meteorology and Climatology*, 55(1), 173–196. Retrieved from <https://doi.org/10.1175/JAMC-D-15-0156.1> doi: 10.1175/JAMC-D-15-0156.1
- Richter, J. H., Sassi, F., & Garcia, R. R. (2010). Toward a physically based gravity wave source parameterization in a general circulation model. *J. Atmos. Sci.*, 67, 136–156. doi: dx.doi.org/10.1175/2009JAS3112.1
- Rignot, E., & Mouginot, J. (2012). Ice flow in greenland for the international polar

- 1154 year 2008–2009. *Geophysical Research Letters*, 39(11).
- 1155 Roeckner, E., Brokopf, R., Esch, M., Giorgetta, M., Hagemann, S., Kornblueh, L.,
 1156 ... Schulzweida, U. (2006). Sensitivity of simulated climate to horizontal
 1157 and vertical resolution in the echam5 atmosphere model. *Journal of Climate*,
 1158 19(16), 3771–3791.
- 1159 Sellevold, R., Van Kampenhout, L., Lenaerts, J., Noël, B., Lipscomb, W. H., &
 1160 Vizcaino, M. (2019). Surface mass balance downscaling through elevation
 1161 classes in an earth system model: Application to the greenland ice sheet. *The
 1162 Cryosphere*, 13(12), 3193–3208.
- 1163 Serreze, M. C., Barrett, A. P., Slater, A. G., Steele, M., Zhang, J., & Trenberth,
 1164 K. E. (2007). The large-scale energy budget of the arctic. *Journal of Geophysical
 1165 Research: Atmospheres*, 112(D11).
- 1166 Simmons, A. J., & Jiabin, C. (1991). The calculation of geopotential and
 1167 the pressure gradient in the ECMWF atmospheric model: Influence on
 1168 the simulation of the polar atmosphere and on temperature analyses.
 1169 *Quart. J. Roy. Meteor. Soc.*, 117(497), 29–58. Retrieved from <https://rmetsonlinelibrary.wiley.com/doi/abs/10.1002/qj.49711749703> doi:
 1170 <https://doi.org/10.1002/qj.49711749703>
- 1171 Small, R. J., Bacmeister, J., Bailey, D., Baker, A., Bishop, S., Bryan, F., ... Verten-
 1172 stein, M. (2014). A new synoptic scale resolving global climate simulation
 1173 using the community earth system model. *J. Adv. Model. Earth Syst.*, 6(4),
 1174 1065–1094. doi: 10.1002/2014MS000363
- 1175 Suarez, M. J., & Takacs, L. L. (1995). Volume 5 documentation of the aries/geos dy-
 1176 namical core: Version 2.
- 1177 Taylor, M. A., & Fournier, A. (2010). A compatible and conservative spectral el-
 1178 ement method on unstructured grids. *J. Comput. Phys.*, 229(17), 5879 - 5895.
 1179 doi: 10.1016/j.jcp.2010.04.008
- 1180 Taylor, M. A., Guba, O., Steyer, A., Ullrich, P. A., Hall, D. M., & Eldred, C.
 1181 (2020). An energy consistent discretization of the nonhydrostatic equations
 1182 in primitive variables. *Journal of Advances in Modeling Earth Systems*, 12(1).
 1183 doi: 10.1029/2019MS001783
- 1184 Taylor, M. A., Tribbia, J., & Iskandarani, M. (1997). The spectral element method
 1185 for the shallow water equations on the sphere. *J. Comput. Phys.*, 130, 92–108.
- 1186 Team, E. J. S., Balaji, V., Boville, B., Collins, N., Craig, T., Cruz, C., ... others
 1187 (2021). *Esmf user guide* (Tech. Rep.).
- 1188 Tedesco, M., & Alexander, P. (2013). Modis (mod10a1) albedo data on the mar rcm
 1189 grid (2000–2013). URL: <https://cds.climate.copernicus.eu>. doi: 10.18739/
 1190 A2SK7T
- 1191 Ullrich, P. A., & Taylor, M. A. (2015). Arbitrary-order conservative and consis-
 1192 tent remapping and a theory of linear maps: Part i. *Monthly Weather Review*,
 1193 143(6), 2419–2440.
- 1194 Ullrich, P. A., Zarzycki, C. M., McClenny, E. E., Pinheiro, M. C., Stansfield, A. M.,
 1195 & Reed, K. A. (2021). Tempestextremes v2. 1: a community framework for
 1196 feature detection, tracking and analysis in large datasets. *Geoscientific Model
 1197 Development Discussions*, 1–37.
- 1198 Van Angelen, J., Lenaerts, J., Lhermitte, S., Fettweis, X., Kuipers Munneke, P.,
 1199 Van den Broeke, M., ... Smeets, C. (2012). Sensitivity of greenland ice
 1200 sheet surface mass balance to surface albedo parameterization: a study with a
 1201 regional climate model. *The Cryosphere*, 6(5), 1175–1186.
- 1202 van Kampenhout, L., Lenaerts, J. T., Lipscomb, W. H., Lhermitte, S., Noël, B.,
 1203 Vizcaíno, M., ... van den Broeke, M. R. (2020). Present-day greenland ice
 1204 sheet climate and surface mass balance in cesm2. *Journal of Geophysical
 1205 Research: Earth Surface*, 125(2).
- 1206 Van Kampenhout, L., Rhoades, A. M., Herrington, A. R., Zarzycki, C. M., Lenaerts,
 1207 J., Sacks, W. J., & Van Den Broeke, M. R. (2019). Regional grid refinement

- in an earth system model: impacts on the simulated greenland surface mass balance. *The Cryosphere*, 13(6), 1547–1564.
- Wan, H., Giorgetta, M. A., Zängl, G., Restelli, M., Majewski, D., Bonaventura, L., ... others (2013). "the icon-1.2 hydrostatic atmospheric dynamical core on triangular grids, part i: formulation and performance of the baseline version". *Geosci. Model Dev.*, 6, 735–763.
- Williamson, D. (2007). The evolution of dynamical cores for global atmospheric models. *J. Meteor. Soc. Japan*, 85, 241-269.
- Williamson, D. (2008). Convergence of aqua-planet simulations with increasing resolution in the community atmospheric model, version 3. *Tellus A*, 60(5), 848–862. doi: 10.1111/j.1600-0870.2008.00339.x
- Zarzycki, C. M., Jablonowski, C., & Taylor, M. A. (2014). Using variable-resolution meshes to model tropical cyclones in the community atmosphere model. *Mon. Wea. Rev.*, 142(3), 1221-1239. doi: 10.1175/MWR-D-13-00179.1
- Zhang, G., & McFarlane, N. (1995). Sensitivity of climate simulations to the parameterization of cumulus convection in the canadian climate center general-circulation model. *ATMOSPHERE-OCEAN*, 33(3), 407-446.

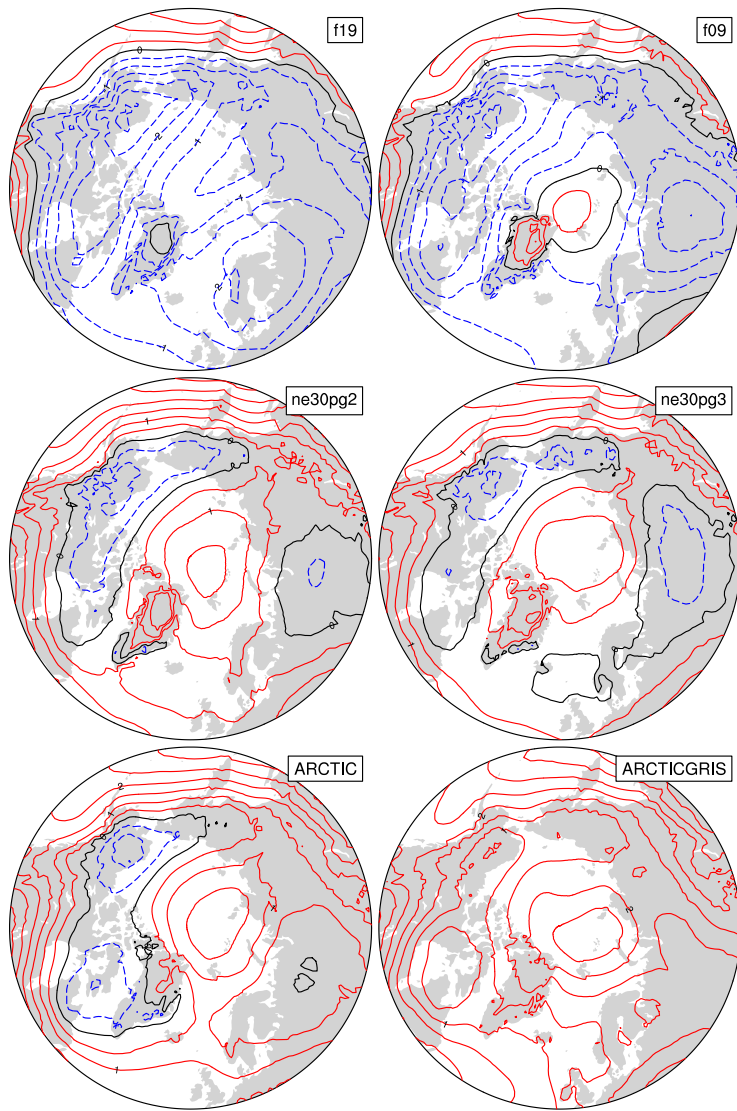


Figure 6. 1979-1998 lower troposphere, northern hemisphere summer virtual temperature biases, computed as the difference from ERA5. Lower troposphere layer mean virtual temperature is derived from the 1000 hPa - 500h Pa geopotential thickness, using the hypsometric equation. Differences are computed after mapping the ERA5 data to the finite-volume grids since the geopotential field is only available on the output tapes in the spectral-element runs that have been interpolated to the f09 grid, inline.

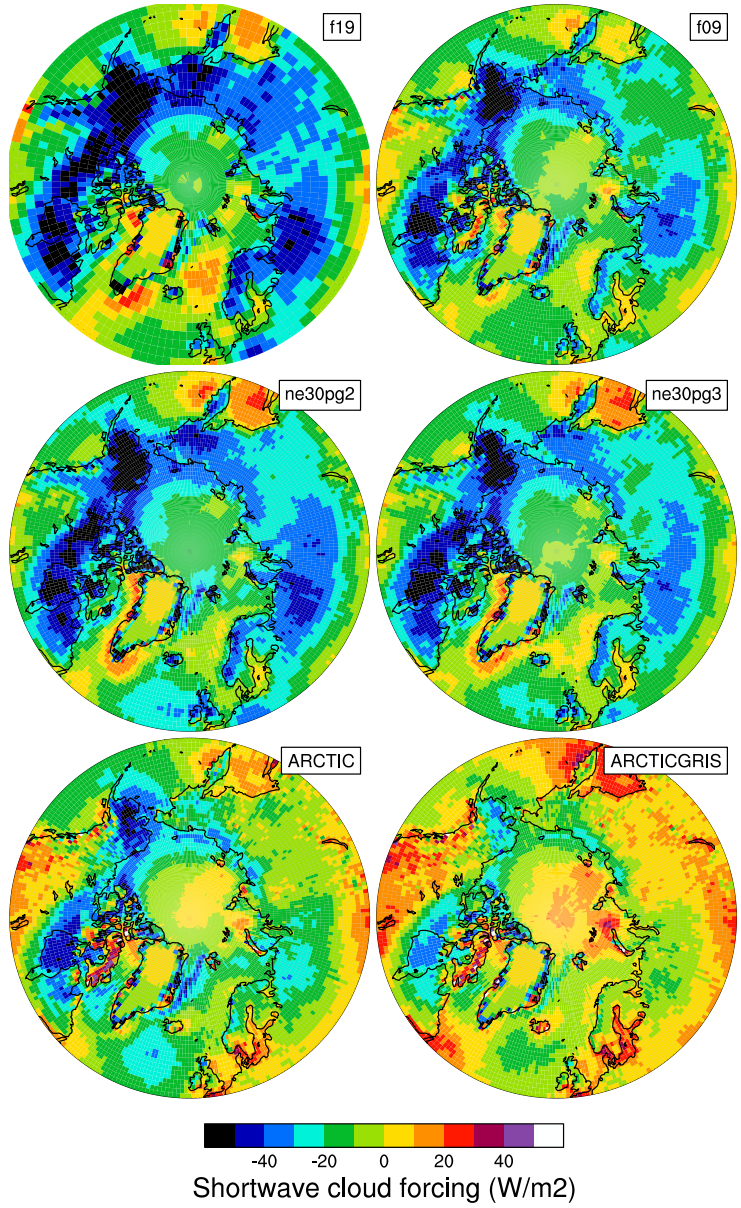


Figure 7. 1979-1998 Northern Hemisphere summer shortwave cloud forcing bias, relative to the CERES-EBAF gridded dataset. Shortwave cloud forcing is defined as the difference between all-sky and clear-sky net shortwave fluxes at the top of the atmosphere. Differences are computed after mapping all model output to the 1° CERES-EBAF grid.

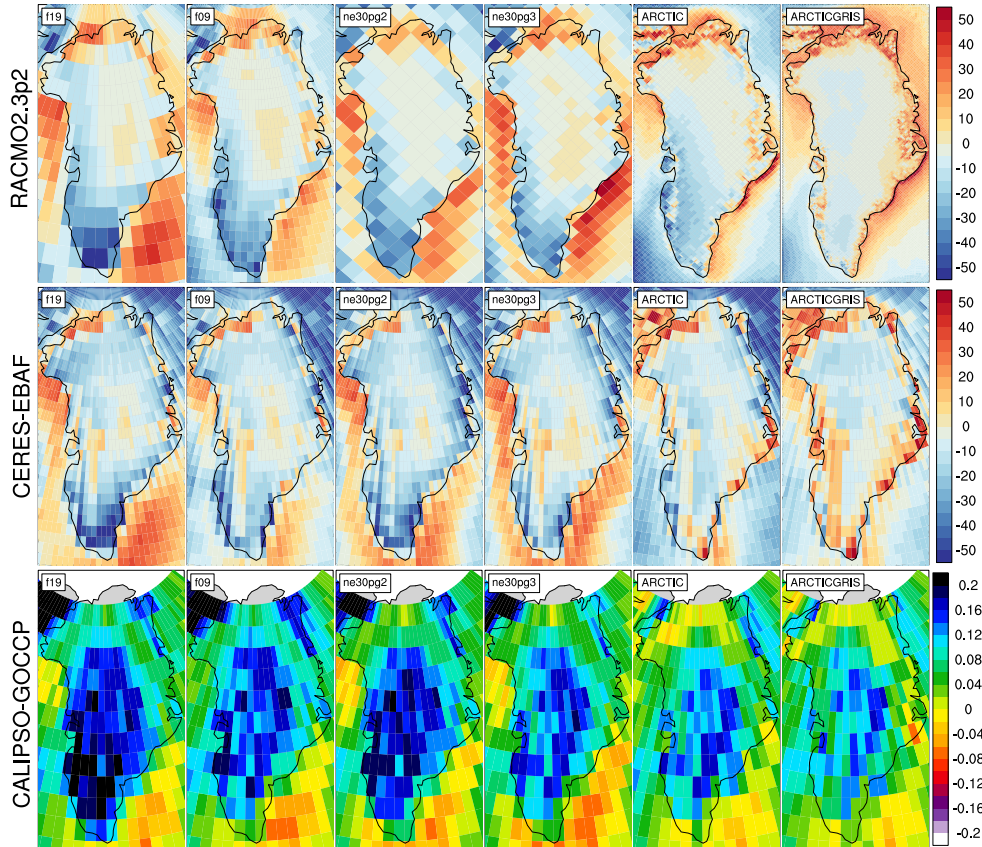


Figure 8. 1979-1998 northern hemisphere summer surface incident shortwave radiation bias (W/m^2), computed as the difference (top) from RACMO2.3p2, and (middle) the CERES-EBAF dataset, and the (bottom) total cloud fraction bias relative to the CALIPSO dataset. CALIPSO and CERES differences are found by mapping the model output to the 1° grid, and differences in the bottom panel are computed after mapping the RACMO2.3p2 dataset to the individual model grids. Note that the averaging period for the CALIPSO-GOCCP and CERES-EBAF panels, 2006-2017 and 2003-2020, respectively, are different from the averaging period for the model results.

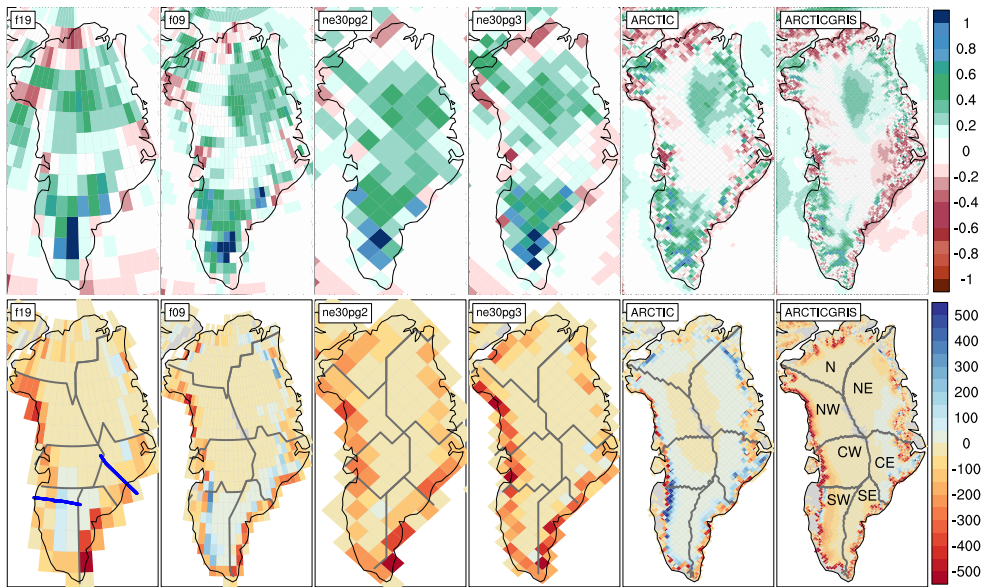


Figure 9. 1979-1998 (top) annual precipitation and (bottom) ice/snow melt biases relative to RACMO2.3p2, evaluated on the native model grids. The precipitation biases are expressed as fractional changes, whereas the melt biases are absolute changes (mm/yr). In the bottom panel, the Rignot and Mouginot (2012) basin boundaries are shown in grey for each model grid. Note that Figure 11 uses the basin boundaries for the two common ice masks, shown in the **f19** and **ne30pg2** panels, in computing the basin-scale integrals. Blue lines in the **f19** panel show the location of the two transects plotted in Figure 12.

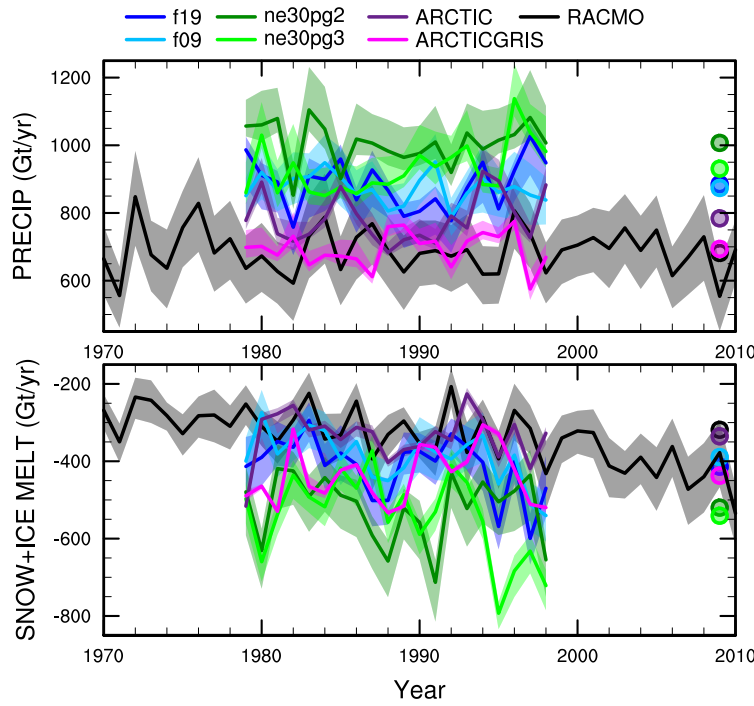


Figure 10. Time-series of annual (solid+liquid) precipitation (top) and annual runoff (bottom) integrated over the Greenland Ice Sheet for all six simulations and compared to the RACMO datasets. The time-series were generated using the common ice mask approach, which results in up to 4 ensembles, with the mean value given by the solid line and shading spanning the extent of the ensemble members.

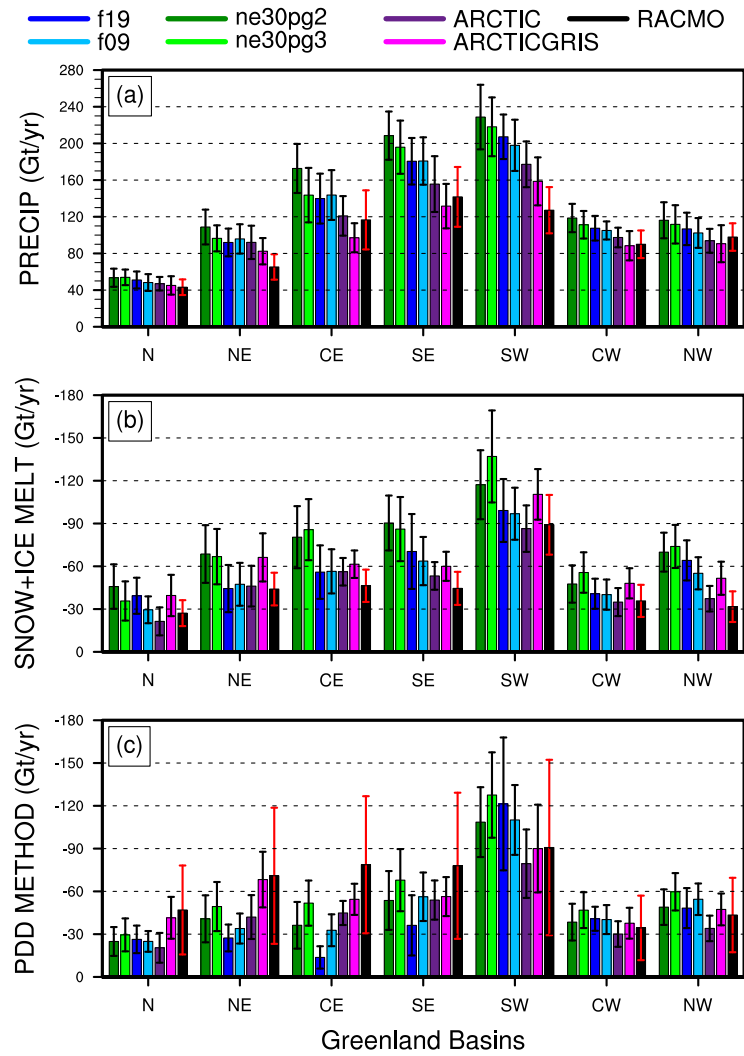


Figure 11. 1979–1998 basin integrated components of the SMB; (top) precipitation, (middle) ice/snow melt and (bottom) ice/snow melt estimated from the PDD method. Whiskers span the max/min of the four ensemble members generated from the common-ice-mask approach. Basin definitions are after Rignot and Mouginot (2012), and are found on the common ice masks using a nearest neighbor approach, and shown in Figure 9.

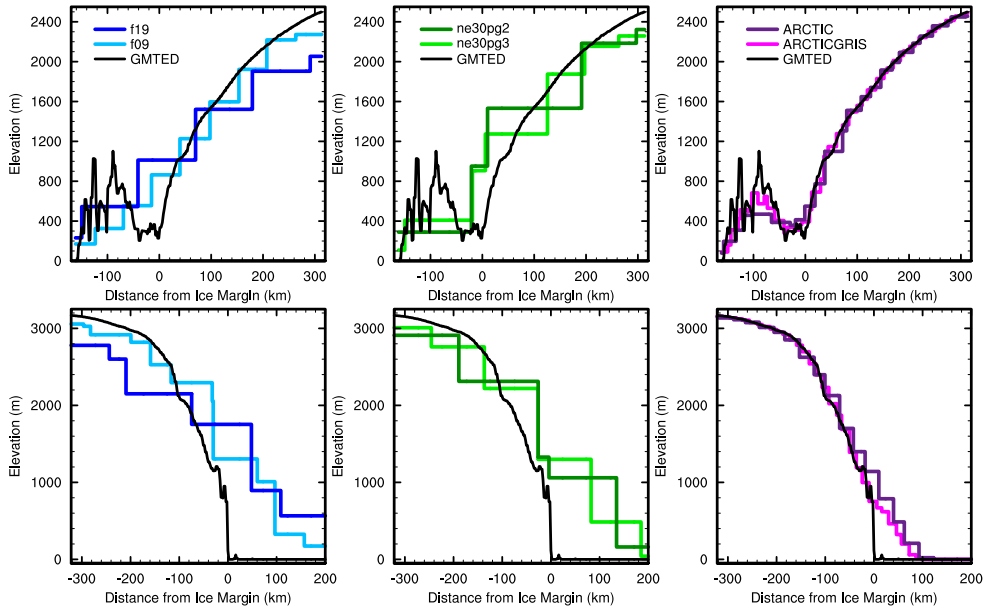


Figure 12. Model surface elevation along the (top) K-transect, and (bottom) a transect spanning the central dome down to the Kangerlussuaq glacier in southeast Greenland, for all model grids. The GMTED reference surface is a 1 km surface elevation dataset (J. Danielson & Gesch, 2011) used for generating the CAM topographic boundary conditions.

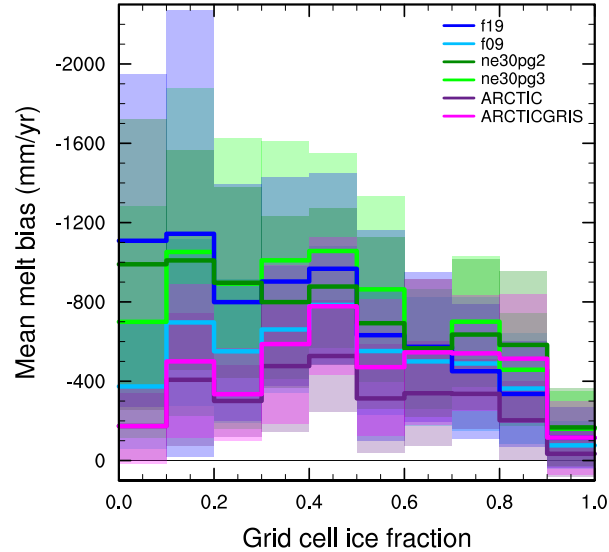


Figure 13. Fractional melt bias over the GrIS, computed relative to the RACMO datasets using the common ice mask approach, and conditionally sampled by grid cell ice fraction provided by the common ice masks. Solid lines are the mean of the distribution with \pm one standard deviation expressed by shading.

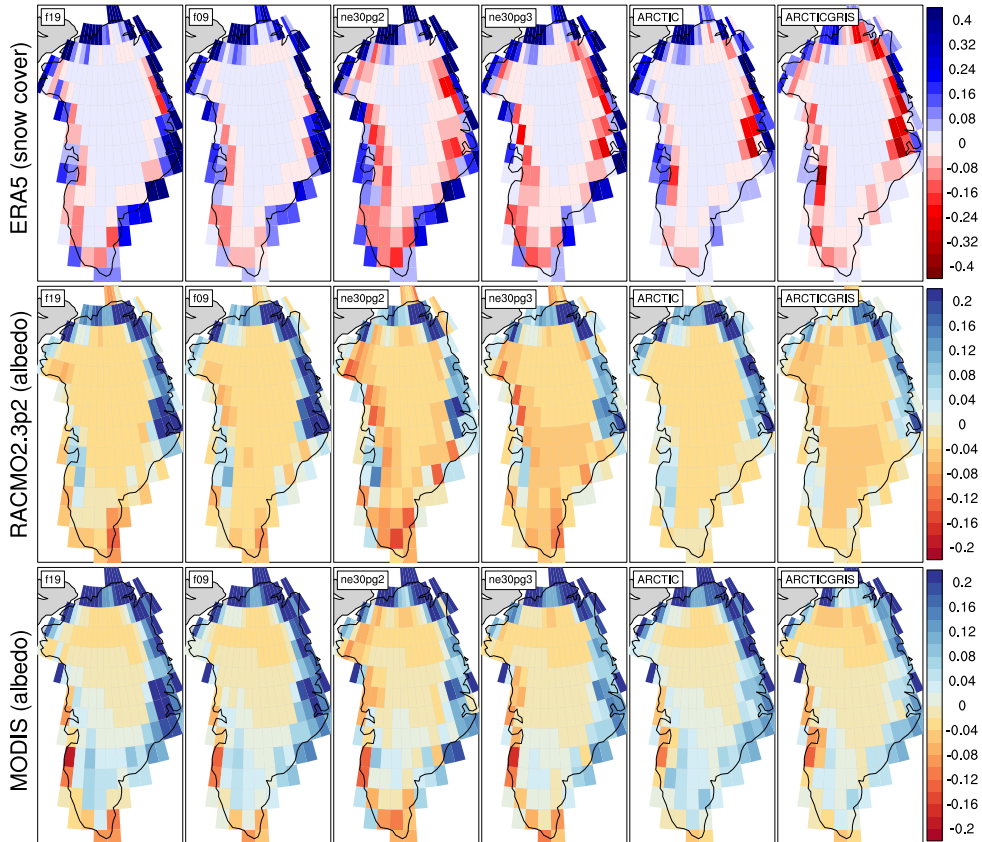


Figure 14. (Top) 1979-1998 bias in northern hemisphere summer snow cover (fraction) relative to ERA4. (Middle and bottom) 1979-1998 summer albedo bias (fraction), computed as the difference (middle) from RACMO2.3p2, and (bottom) the MODIS dataset of Tedesco and Alexander (2013). All model and validation data have been mapped to the f19 grid to facilitate the comparison across the different grids.

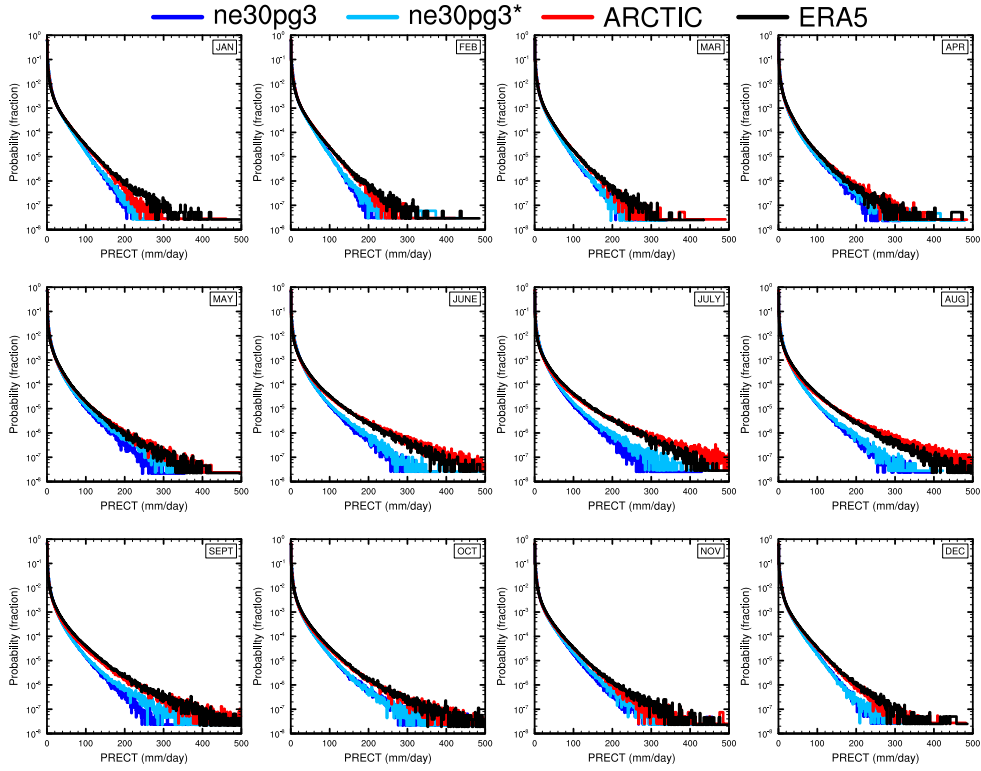


Figure 15. PDFs of the total precipitation rate associated with tracked storms, by month, in the ne30pg3, ne30pg3* and Arctic runs, and compared with the ERA5 dataset.

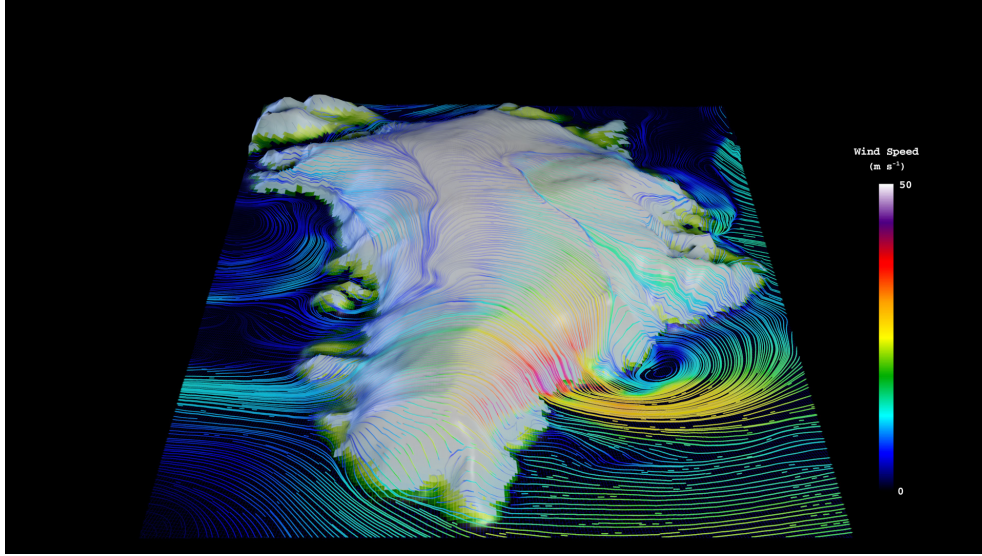


Figure 16. Snapshot of the lowest model level streamlines from the Arctic – GrIS visualization, with color shading denoting the wind magnitude.

OMEGA500, 1 year average, F2000climo, 32 levels

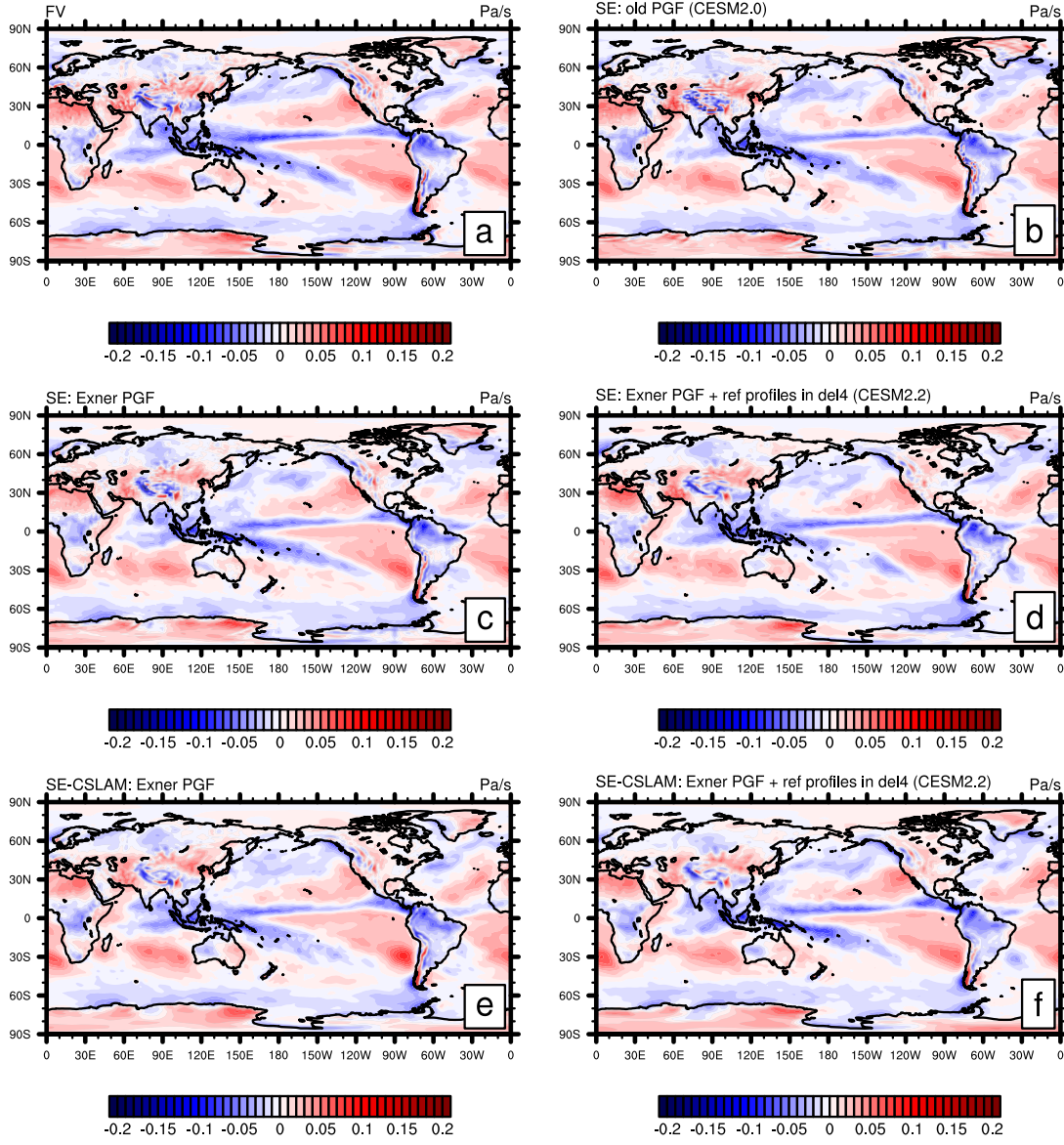


Figure A1. One year averages of vertical pressure velocity at 500hPa (OMEGA500) using (a) CAM-FV (Finite-Volume dynamical core) and (b-f) various versions of the spectral-element (SE) dynamical core at approximately 1° horizontal resolution and using 32 levels. (b) is equivalent to the CESM2.0 version of the SE dynamical core using the "traditional"/"old" discretization of the pressure-gradient force (PGF). Plot (c) is equivalent to configuration (b) but using the Exner form of the PGF. Plot (d) is the same as configuration (c) but also subtracting reference profiles from pressure and temperature before applying hyperviscosity operators (which is equivalent to the CESM2.2 version of SE in terms of the dynamical core). Plots (e) and (f) are equivalent to (c) and (d), respectively, by using the SE-CSLAM (ne30pg3) version of the SE dynamical core (i.e. separate quasi-uniform physics grid and CSLAM transport scheme).

OMEGA500, 18 months average, FHS94 forcing, 32 levels

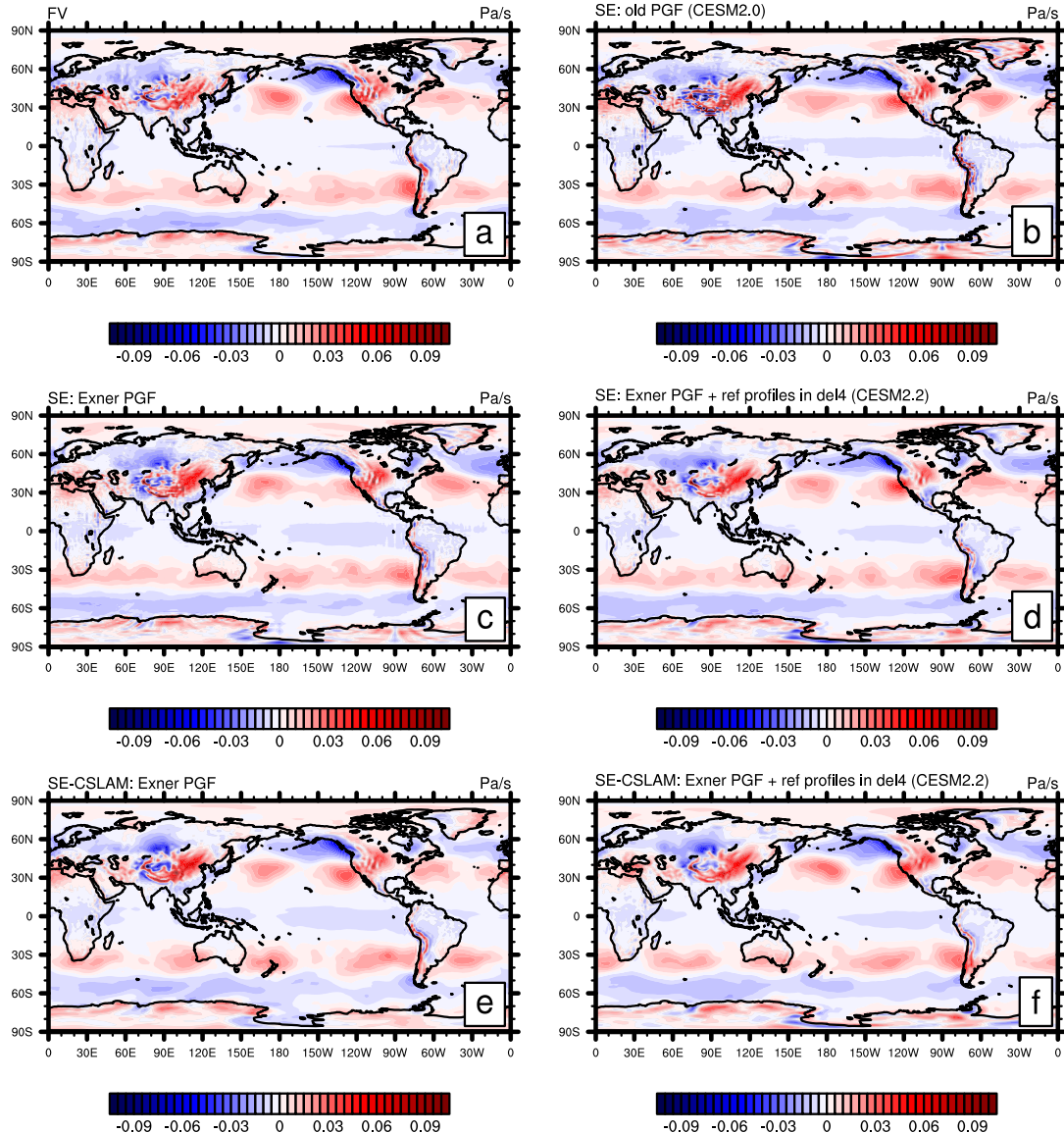


Figure A2. Same as Figure A1 but using modified Held-Suarez forcing and the average is over 18 months (excl. spin-up).